https://doi.org/10.5194/egusphere-2024-4073
Preprint. Discussion started: 27 January 2025

Formation and composition of organic aerosols from the uptake of glyoxal on natural mineral dust aerosols: a laboratory study

Francesco Battaglia[1], Paola Formenti[1], Chiara Giorio[2], Mathieu Cazaunau[3], Edouard Pangui[3], Antonin Bergé[3], Aline Gratien[1], Thomas Bertin[3], Joel F. de Brito[4], Manolis N. Romanias[4], Vincent Michoud[1], Clarissa Baldo[1,3], Servanne Chevaillier[3], Gael Noyalet[3], Philippe Decorse[5], Bénédicte Picquet-Varrault[3], and Jean-François Doussin[3]

[1] Université Paris Cité and Univ Paris Est Créteil, CNRS, LISA, F-75013 Paris, France
[2] Yusuf Hamied Department of Chemistry, University of Cambridge, Lensfield Road, Cambridge, CB2 1EW, UK
[3] Univ Paris Est Créteil and Université Paris Cité, CNRS, LISA, F-94010 Créteil, France
[4] IMT Nord Europe, Institut Mines-Télécom, Université de Lille, Centre for Energy and Environment, 59000, Lille, France
[5] Université Paris Cité, CNRS, Itodys, F-75013 Paris, France

Corresponding author: P. Formenti (paola.formenti@lisa.ipsl.fr)

Abstract

The uptake of glyoxal on realistic submicron mineral dust aerosol particles from a natural soil (Gobi Desert) is investigated during experiments in a large simulation chamber, under variable experimental conditions of relative humidity, irradiation, and ozone concentrations. The uptake of glyoxal on the dust particles starts as soon as the glyoxal is injected in the chamber. At 80% RH, the measured uptake coefficient of glyoxal on mineral dust is $\gamma = (9 \pm 5) \times 10^{-3}$. The totality of the mass of reacting glyoxal is transformed in organic matter on the surface of the dust particles. The uptake of glyoxal is accompanied by the appearance marker peaks in the organic mass spectra and a persistent growth in the volume concentration of the dust particles. While the mass of the organic matter on the dust rapidly reverts to values prior to uptake, the organic composition of the dust is modified irreversibly. Glycolic and other organic acids but also oligomers are detected on the dust. At 80% RH, compounds ranging from C_4 to C_{10} are observed as oligomerization products of glyoxal mono- and di-hydrate forms. The study suggests that dust aerosols could play a very substantial role in the formation of organic aerosols at high relative humidity, but also that the reaction could have potential important implications for the dust optical and hygroscopic properties, including their pH.

https://doi.org/10.5194/egusphere-2024-4073
Preprint. Discussion started: 27 January 2025

1 Introduction

Mineral dust originates naturally from the wind erosion of arid or semi-arid soils, resulting in the suspension of particles with diameters from fractions to hundreds of microns, which can be transported over thousands of kilometres whilst in the atmosphere (Adebiyi et al., 2023; Mahowald et al., 2014). The total global mass of mineral dust particles emitted annually in the atmosphere is of the order of 4600 Tg yr^{-1}, accounting for approximately 40% of the total annual aerosol emissions (Knippertz and Stuut, 2014; Kok et al., 2021). Major natural source areas of mineral dust are North Africa (~50% of the global annual dust emissions), Asia (~40%), North America, and the Southern Hemisphere (~10%; Kok et al., 2023). Anthropogenic emissions are associated with soil erosion for agriculture, pasture, and deforestation (Tegen and Fung, 1995; Webb and Pierre, 2018), but their contribution to the total annual dust mass loading is uncertain, ranging from 5 to 60% (Chen et al., 2023). Mineral dust significantly impacts the Earth's energy balance by absorbing and scattering radiation in the solar and terrestrial spectra (Di Biagio et al., 2019; Kok et al., 2023) and by influencing the lifetime and optical properties of mixed-phase and ice clouds (e.g., Atkinson et al., 2013; Harrison et al., 2001; Steinke et al., 2016). Current estimates of the effective radiative forcing (sum of direct and indirect) of natural mineral dust are in the range of -0.07 ± 0.18 W m^{-2} (Kok et al., 2023), owing to large uncertainties in the atmospheric mass loading and properties of dust at emission and during transport (Castellanos et al., 2024; Li et al., 2021).

Gas-particle interactions along the dust lifecycle contribute to these uncertainties. Numerous laboratory and field studies show that mineral dust is capable to adsorb various reactive gaseous compounds, which may modify its chemical composition, and in turn to alter optical properties, hygroscopicity and ice nucleation activity but also may affect the oxidative capacity of the atmosphere (Bauer et al., 2007; Chirizzi, 2017; Crowley et al., 2010; Joshi et al., 2017; Liu et al., 2013; Ooki and Uematsu, 2005; Romanias et al., 2012; Seisel et al., 2004; Tang et al., 2017; Turpin and Huntzicker, 1995; Usher et al., 2003; Wagner et al., 2008). Dust aerosol may promote photocatalytic reactions of inorganic gases such as SO_2 and NO_2, initiating nucleation events (Dupart et al., 2012; Nie et al., 2014).

The uptake of volatile organic compounds (VOCs) on mineral dust such as limonene, toluene (Romanías et al., 2016), isoprene (Zeineddine et al., 2017), phenol

https://doi.org/10.5194/egusphere-2024-4073
Preprint. Discussion started: 27 January 2025

(Hettiarachchi and Grassian, 2024), and dicarboxylic acids (Ponczek et al., 2019), is also documented. These reactions may alter the VOC budget in the atmosphere and lead to the formation of secondary organic aerosols (Li et al., 2019; Tang et al., 2017; Usher et al., 2003; Xu et al., 2023; Zeineddine et al., 2023), one of the key player of atmospheric chemistry (Shrivastava et al., 2017).

Glyoxal (CHOCHO) is one of the most abundant VOCs in the troposphere (Lewis et al., 2020). Atmospheric glyoxal is produced through the oxidation of aromatic compounds like benzene, toluene, and p-xylene (Volkamer et al., 2001) as well as by the photochemical oxidation of isoprene (Chan et al., 2017). The global atmospheric concentrations have been evaluated in the range of 10 – 100 pptv by Fu et al. (2008). However, case studies show sometimes higher concentrations. During a field study in Shanghai in the summer of 2018, Guo et al. (2021) reported an average glyoxal concentration of 164 ± 73 pptv, due to daytime photochemistry. Local concentrations of up to 400 pptv have been documented in regions influenced by aromatic pollution (Li et al., 2022). Satellite measurements of glyoxal show that the highest concentrations in tropical and sub-tropical regions are found during warm, dry periods influenced by biogenic emissions and vegetation fires, but also anthropogenic pollution (Vrekoussis et al., 2009). Elevated glyoxal concentrations have been observed in aged biomass burning plumes and tropical ocean regions, revealing model under-predictions in high-emission areas due to missing complex organic compound sources (Kluge et al., 2023). Field measurements in the north east Atlantic Ocean reveal that models generally underestimate glyoxal concentrations due to missing contributions from acetaldehyde and other chemical precursors, and a potential glyoxal source from the ocean surface organic microlayer, particularly significant at night (Walker et al., 2022).

Glyoxal is a very soluble molecule which readily oligomerises in water, leading to the formation of larger molecules (Kalberer et al., 2004; Shapiro et al., 2009). It also has the ability to uptake onto aerosol particles, potentially serving as a significant source of organic aerosols (e.g., Liggio et al., 2005b, Carlton et al., 2007; Ervens and Volkamer, 2010; Galloway et al., 2009; Knote et al., 2014). The uptake of glyoxal on ammonium sulphate particles can lead to the formation of carbon-nitrogen compounds (such as imidazole derivatives), oligomers, and organic acids (Galloway et al., 2009), that has been observed to cause their browning (De Haan et al., 2020). The light-

https://doi.org/10.5194/egusphere-2024-4073
Preprint. Discussion started: 27 January 2025

absorbing imidazole derivatives formed by glyoxal have been found to act as a photosensitizer, initiating radical chemistry under realistic irradiation conditions in the aerosol phase and initiating aerosol growth in the presence of limonene (Rossignol et al., 2014).

Shen et al. (2016) revealed that glyoxal can also uptake onto synthetic minerals proxies of natural mineral dust, forming oligomers, organo-sulphates, formic acid, and glycolic acid, henceforth suggesting a potential significant mechanism for organic aerosol formation and modification of the optical and hygroscopic properties of mineral dust.

Following up from the pioneering study by Shen et al. (2016), in this paper we present the results of laboratory experiments using a large-scale simulation chamber to investigate the formation of OA from the uptake of glyoxal on realistic airborne mineral dust particles. Dust aerosols are generated from a natural parent soil from the Gobi Desert, one of the most important sources of tropospheric dust and representative of an area where this interaction could take place (Wang et al., 2015).

This paper has two major objectives. First, it provides experimental observations of the uptake of glyoxal on mineral dust aerosol, leading to the formation of organic aerosol mass upon interaction and measuring glyoxal uptake coefficient of mineral dust. Secondly, it presents the chemical composition of the mixed organic-dust aerosols, in terms of its oxidation state, molecular composition and the evolution of secondary organic aerosol content from glyoxal.

2 Experimental

This study uses the CESAM atmospheric simulation chamber, a 4.2 m^3 cylindrical stainless-steel reactor initially described by Wang et al. (2011). CESAM is specifically designed to study multiphase processes involving aerosol particles, gas-phase compounds and water, both in the vapour and liquid phases (Brégonzio-Rozier et al., 2016; Denjean et al., 2014; Giorio et al., 2017). CESAM is equipped with three 6.5 kW high-pressure arc xenon lamps (model EX-170GM3-E, IREM SpA, Borgone, Italy) and 6 mm Pyrex plate filters to mimic the solar radiation. A 50 cm stainless-steel four-blade fan located at the bottom of the chamber ensures a mixing time of about 1 minute for the gas phase and the homogeneity of the internal composition.

The ageing experiments last up to five hours. Before each experiment, the chamber is evacuated down to 10^{-4} mbar. The chamber is then filled with a mixture of 80% N_2

https://doi.org/10.5194/egusphere-2024-4073
Preprint. Discussion started: 27 January 2025

(Messer, purity > 99.995%) and 20% O_2 (Linde, 5.0) to an internal pressure exceeding by about 5 to 10 mbar the local atmospheric pressure, to prevent accidental contamination during the experiments. For the experiments carried out in wet conditions, the injection of water vapour precedes the injection of dust. The injection of glyoxal (1 ppmv) was conducted at least after 30 minutes after the dust to ensure that the dust particles are homogenously distributed. Irradiation is started within one hour after the glyoxal uptake onto the particles. Ozone is used to verify the sensitivity of the reactions to the presence of an oxidant. For those experiments, ozone is injected before glyoxal.

2.1 Experimental protocols

Dust aerosols are generated and injected into the chamber according to the protocol detailed in Battaglia et al. (2024). The natural soil sample used in this study is from the Gobi Desert (107.48°N; 36.49°E). Prior use, the soil is sieved at 1000 µm and dried at 100°C for less than an hour to remove adsorbed water and contamination from volatile gases. A quantity ranging from 30 and 50 g is placed in a 1 L Büchner flask and shaken at 100 Hz using a sieve shaker (Retsch® AS200) to simulate the saltation and sandblasting mechanisms through which wind erosion generates airborne dust in the real atmosphere (Di Biagio et al., 2017). An Aerodynamic Aerosol Classifier (AAC, Cambustion®) is placed between the dust generator and the chamber to inject mono-modal dust centred between 300 and 400 nm in geometric diameter.

Glyoxal is prepared by heating a mixture of equal amounts of its trimer hydrate (Fluka® Analytical) and P_2O_5 (Sigma – Aldrich ReagentPlus®, 99%) at 150°C (Horowitz et al., 2001). The trimer decomposition occurs inside a vial connected to a vacuum gas manifold. Glyoxal is collected as yellow crystals in a second vial immersed in an ethanol – liquid nitrogen cold trap at around -90°C and then vaporised in a 2.1 L glass bulb to a controlled pressure. This vial is connected to the simulation chamber to inject the glyoxal through a nitrogen flow.

Ozone is generated by a Corona discharge in pure O_2 using a commercial dielectric ozone generator (MBT 802N, Messtechnik GmbH, Stahnsdorf, Germany). Water vapour is generated by heating ultrapure water (Milli-Q IQ 7000, Merk™) inside a pressurised stainless-steel vessel, previously rinsed at least three times. The total organic carbon (TOC) content of the ultrapure water is monitored in each experiment

https://doi.org/10.5194/egusphere-2024-4073
Preprint. Discussion started: 27 January 2025

to evaluate the influence on the production of organic particles, which was found to be minor (see Text S1 in the Supplementary Material). The relative humidity (RH) inside the chamber is measured by a HMP234 Vaisala® humidity and temperature transmitter.

2.2 Measurements and instrumentation

2.2.1 Gas-phase composition

CESAM is equipped with an in-situ long-path FTIR spectrometer (Bruker Tensor 37), which enables the collection of spectra with a time resolution of 5 minutes. The spectral range covered is 700 – 4000 cm^{-1}, at a resolution of 0.5 cm^{-1} and an optical path length of 120 meters. To avoid major water interference, glyoxal is quantified by integrating the peak corresponding to the stretching of the C–H bonds, in the 2720 to 2930 cm^{-1} interval. Additional species quantified by FTIR spectroscopy are formic acid (HCOOH), carbon monoxide (CO), and ozone (O_3). HCOOH is quantified by integrating the absorption band centred at 1105 cm^{-1}, associated with the C-O bond vibration typical of the carboxylic group of formic acid. CO is quantified by integrating the typical gas phase stretching absorption centred at about 2143 cm^{-1}, and O_3 is quantified by integrating the absorption band of its asymmetric stretching, centred at about 1043 cm^{-1}.

A CAPS (Cavity Attenuated Phase Shift) NO_2 analyser (Model T500U, from Teledyne API), with a concentration range of 10 – 1000 ppbv and an integration time of 30 s was also connected to the chamber for glyoxal detection. VOCs are monitored by a PTR-ToF-MS (KORE Technology®, second generation) operated in H_3O^+ ionization mode at a time resolution of 1 minute. The reactor pressure and temperature are 1.35 mbar and 60°C, respectively, leading to an E/N ratio of 131 Td, where E is the electric field and N is the concentration of neutral particles. This ratio is used to determine the effectiveness of the ion-molecule collisions and is given in the unit Townsend (Td). Ion signals measured by PTR-MS are normalized by signals of reagent ions (i.e. H_3O+ and H_3O+(H_2O)) to account for variability in instrumental conditions, following equation 5.2.

Additional gas analysers are used to monitor NO_x (APNA-370 Horiba®; measurement range 1 – 1000 ppb; sampling flow 0.8 L min^{-1}; response time 120 s) and CO/CO_2 (APEE ProCeas®; CO_2 limit of detection 5 ppm; CO limit of detection 10 ppb; sampling flow 0.2 L min^{-1}; response time 45 s).

https://doi.org/10.5194/egusphere-2024-4073
Preprint. Discussion started: 27 January 2025

2.2.2 Aerosol total number concentration and size distribution

The aerosol total number concentration above 2.5 nm is measured by a Condensation Particle Counter Condensation Particle Counter (TSI® model 3075, sampling time 1 s, operated at 1.5 L min^{-1}). The aerosol number size distribution is measured by a combination of a Scanning Mobility Particle Sizer (SMPS) consisting of a Differential Mobility Analyser (TSI®, model 3080) coupled with a Condensation Particle Counter (TSI® model 3072, sampling time 180 s, operated at 0.3/3.0 L min^{-1} aerosol flow/sheath flow) measuring particles with mobility diameters between 19.5 and 881.7 nm (107 size channels) and an Optical Particle Counter (sky-GRIMM® OPC model 1.109, sampling flow=1.2 L min^{-1}, laser wavelength = 655 nm, sampling time 12 s) measuring particles with optical mobility diameters between 0.265 µm to 31 µm (31 size channels).

The procedure for combining the aerosol size distributions measured by the SMPS and the sky-GRIMM® OPC is based on the method by Baldo et al. (2023), as described in detail in Battaglia et al. (2024). The number size distributions, expressed in dN/dlog$D$ (cm^{-3}), are used to evaluate the total particle surface S (µm^2 cm^{-3}) and volume V (µm^3 cm^{-3}) by assuming spherical particles as

$$S = \int \pi D^2 \frac{\mathrm{d}N}{\mathrm{dlog}D}\ \mathrm{dlog}D \tag{1}$$

$$V = \int \frac{\pi}{6}\ D^3 \frac{\mathrm{d}N}{\mathrm{dlog}D}\ \mathrm{dlog}D \tag{2}$$

2.2.3 Aerosol chemical composition

The aerosol chemical composition is measured by a combination of online and offline methods.

2.2.3.1 Time-of-flight Aerosol Chemical Speciation Monitor

A Time-of-flight Aerosol Chemical Speciation Monitor (ToF–ACSM; Aerodyne Research Inc., Billerica, Massachusetts) equipped with a standard vaporiser provides quantitative unitary mass resolution spectra of OA submicronic particles (40 nm–1 µm in vacuum aerodynamic diameter). Particles are sampled with a time resolution of 6 minutes and a flow of 0.85 L min^{-1} through a Nafion membrane dryer (model PD-50T-12) installed upstream of the ToF–ACSM. The incoming aerosol is thermally vaporised

https://doi.org/10.5194/egusphere-2024-4073
Preprint. Discussion started: 27 January 2025

at ~600°C. The resulting gas is ionised by electron impact ionization (EI) and the fragments are classified by the time-of-flight mass analyser.

Data processing (including mass calibration, peaks integration and air beam correction of ion intensities) is conducted with Tofware version 3_2_40209, the ACSM data analysis package for the software Igor Pro 7.08 (Wavemetrics, Inc., Portland, OR, USA). The organic mass concentration m_{org} is obtained considering a unitary collection efficiency (CE = 1) and a relative ionization efficiency (REI) of 1.4 (Nault et al., 2023). This applies also for the organic linked to mineral dust.

Given that the glyoxal fragment CH_2O^+ (*m/z* =30) has an isobaric interference with the NO^+ fragment from nitrate, the contribution of glyoxal to the organic signal at 30 *m/z* is estimated with a minor modification of the standard fragmentation table made following the method proposed by Galloway et al. (2009) in their study of glyoxal uptake on ammonium sulphate (AS) particles. The contribution to the total signal at 30 *m/z* from nitrate is imposed to be 1.7 times the intensity of the nitrate signal at 46 *m/z*, which corresponds to the 30/46 signal ratio measured during nitrate calibration. The contribution to 30 *m/z* of the organic is then the total signal minus the contribution of the nitrate and the contribution of air. The elemental ratios of the organic fraction O/C and H/C are calculated from the measured f_{44} and f_{43} respectively, following the parametrizations proposed by Aiken et al. (2008) and Ng et al. (2011), respectively.

2.2.3.2. Filter sampling

Filter samples are collected using a custom-made stainless-steel holder (6 mm diameter to concentrate particles on a small surface) operated at 10 L min^{-1} and preceded by an active charcoal denuder to remove ozone and VOCs. The sampling time ranges from 30 minutes to 3 hours. Particles are collected on PTFE filters (Zefluor, 47 mm diameter, 2 µm pore size, Pall Life Sciences), and quartz fibre filters (Tissuquartz 2500 QATUP, 47 mm diameter, Pall Life Sciences). Before sampling, the PTFE filters and filter holders are cleaned with dichloromethane (99.8 %, HPLC grade) in an ultrasonic bath. Quartz filters are pyrolyzed at 550°C for approximately 8 hours. After sampling, filters are folded and placed in an aluminium paper envelope previously pyrolyzed (same protocol as for filters), and stored in a refrigerator at -18°C. For each experiment, one blank sample is collected by sampling for about 20 min from the chamber only filled with N_2 and O_2. Analytical blanks, corresponding to pyrolyzed filters that had not undergone any sampling, were also collected.

https://doi.org/10.5194/egusphere-2024-4073
Preprint. Discussion started: 27 January 2025

2.2.3.3. SFE/GC-MS organic aerosol analysis

Supercritical fluid extraction coupled with gas chromatography mass spectrometry (SFE/GC-MS) is used to analyse the molecular composition of the aerosol organic fraction. It was originally developed by Chiappini et al., 2006 and was slightly modified by a Teledyne ISCO model 260D pump for the extraction and a GC (Clarus 680 PerkinElmer) –MS (Clarus MS SQ8C Perkin Elmer) for the analysis.

The analytical protocol of the SFE/GC-MS analysis begins by placing the quartz filters inside the extraction cell. Prior to the extraction, 5 µL of two different solutions are deposited on the filters using a precision syringe (CR700-20 1-20ul (22s/2”/3), Hamilton, USA): (a) an internal standard solution composed by 20 µg mL^{-1} of Tridecane (99%, Sigma-Aldrich) and o-Toluic acid (Sigma Aldrich, purity >97 %) in dichloromethane (99.8 %, HPLC grade) and (b) a derivatizing agent solution composed by N,O-bis(trimethylsilyl)trifluoroacetamide (BSTFA) and 1% of trimethylchlorosilane as catalyst, provided by Sigma-Aldrich. The first step of the analysis is a static extraction, in which the cell is filled with supercritical CO_2 (LINDE, reference CO_2 High Purity)), that interacts with the filter at 300 bar and 60°C, for 40 min. During this step, the trimethylsilylation of hydroxy and carboxy functions by BSTFA also occurs (generating trimethylsilyl (TMS) derivatives). The supercritical fluid containing the analytes is transferred to the GC injector through a deactivated silica transfer line. The injector is cooled at -20°C using liquid nitrogen flowing around the injector for 15 minutes, where the compounds are retained, and the gaseous CO_2 is removed. Once the extraction step was completed, the chemical analysis was continued with the injection of the condensed compounds by heat flash on the GC injector from -20°C to 280°C. The compounds are then eluted with helium flowing at 1 mL min^{-1} (Linde) and transferred to the GC (Clarus 680 PerkinElmer) for separation. The temperature gradient of the GC column (Rxi®-5Sil MS column (30 m, 0,25mmi.d., film thickness: 0.25 µm, Restek) goes from 60°C to 280°C at a rate of 5°C min^{-1} and held at 280°C for 10 min. Detection is achieved through electron impact (70 eV electron energy) ionisation followed by a quadrupole mass spectrometer (Clarus MS SQ8C Perkin Elmer) analysis that produces mass spectra from m/z 50 to m/z 300.

The data analysis is conducted using the proprietary software (TurboMass Version 6.1.0.1965 PerkinElmer®). The analysis is limited to the chromatographic peaks which elutes before the internal standards (around 42 minutes), as for higher retention times

https://doi.org/10.5194/egusphere-2024-4073
Preprint. Discussion started: 27 January 2025

the signal to noise ratio is lower and not conclusive. The chromatograms of each filter sample are compared with those of the analytical and procedural blanks and a mass spectrum is extracted from each chromatographic peak that is not present in the blank. To account for the method variability in extraction efficiency concentrations are corrected using the internal standard o-Toluic acid TMS derivatives. The structural analysis of the molecule generating every chromatographic peak is then carried out using two methods. Each mass spectrum is compared with the reference spectra of the National Institute of Standards and Technology (NIST) Mass Spectral Library (Version 2.2), which assigns a structure to each spectrum with a relative probability. For spectra for which the automatic structural assignment fails (low assignment probability), we searched for target mass fragments derived from molecules linked to glyoxal reactivity (see Table S1 in the Supplementary Material), in particular the 73 m/z fragment corresponding to a TMS derivatization $[Si(CH_3)_3]^+$, the 147 m/z fragment corresponding to two TMS derivatizations $[(CH_3)_2Si{=}OSi(CH_3)_3]^+$, the 131 m/z fragment (Glyoxylic acid TMS derivatized – CH_3), and 205 m/z fragment (Glyoxal monohydrate – CH_3).

2.2.3.4. Electrospray ionization (ESI) high-resolution mass spectrometry

Molecular analysis of the organic fraction collected on the quartz filters is performed by electrospray ionization (ESI) high-resolution mass spectrometry (Kourtchev et al., 2015). A high-resolution (mass resolution=100000 at *m/z* 400) LTQ Orbitrap Velos mass spectrometer (Thermo Fisher, Bremen, Germany) equipped with a TriVersa Nanomate robotic nanoflow chip-based ESI source (Advion Biosciences, Ithaca NY, USA) is used to obtain high resolution mass spectra of the methanol extracts following an adaptation of the procedure described in Kourtchev et al. (2015). Filters are extracted one time in 1 mL of methanol (Optima TM grade, Fisher Scientific) and two times in 0.5 mL of methanol under ultrasonic agitation in slurry ice for 15 min. Extracts are combined and filtered sequentially through a 0.45 µm pore size and a 0.2 µm pore size Teflon filter (ISODiscTM Supelco), which are then reduced by volume to approximately 50–200 µL under a gentle stream of nitrogen. The resulting sample is injected by direct infusion. The negative ionization mass spectra are collected in three replicates at ranges m/z 50–500 and m/z 150–1000 and processed using Xcalibur 2.1 software (Thermo Scientific). In the settings of the data processing, the following atoms are included in the peak assignment: C (from 1 to 100 atoms in the possible assigned

https://doi.org/10.5194/egusphere-2024-4073
Preprint. Discussion started: 27 January 2025

molecular formula), H (1-200), O (0-50), N (0-5), S (0-2), ^{13}C (0-1) and ^{34}S (0-1). The allowed mass accuracy in the formula assignment is ± 4 ppm.

The peak assignment to a molecular formula is done according to Zielinski et al. (2018). The protocol includes internal calibration, noise removal, blank subtraction, and additional atomic constraints for formula filtering: elemental ratios were set as 0.3 ≤H/C≤ 2.5, O/C≤ 2, N/C≤ 0.5, S/C≤ 0.2, $^{13}C/^{12}C$≤ 0.011 and $^{34}S/^{32}S$≤ 0.045, and nitrogen rule. In the case of multiple assignments for the same peak, the formula with the lowest mass error was kept. This process allowed for the retrieval of parameters describing carbon oxidation, such as O/C and H/C ratios. Consequently, each mass spectrum was analysed to construct a van Krevelen diagram, which is a graphical representation illustrating the sample composition in terms of carbon, oxygen, and hydrogen in the identified molecular formulas (Patriarca et al., 2018). Identified molecular formulas are categorised into the following groups: CHO, CHON, CHOS, CHNS, and CHONS.

A targeted search for molecular formulas resulting from glyoxal reactivity is also done. In this search, we included formulas associated with glyoxal chemical transformations such as hydration, oxidation, and oligomerization. Starting from the glyoxal formula, $C_2H_2O_2$, formulas for mono- and dihydration products are $C_2H_4O_3$ and $C_2H_6O_4$, respectively. Oxidation products included formic acid (CH_2O_2), glycolic acid ($C_2H_4O_3$), glyoxylic acid ($C_2H_2O_3$), and oxalic acid ($C_2H_2O_2$). Oligomers formed by the hydrolysis of hydrated glyoxal formulas were also sought. In the process of hydrolysis-driven oligomerization, each successive molecular addition results in the loss of a water molecule. If the oligomer is a ring, an additional water molecule is lost due to the condensation of the linear oligomer terminations. Denoting n as the number of molecules of the monohydrated form ($C_2H_4O_3$) and m as the number of molecules of the dihydrated glyoxal form ($C_2H_6O_4$) participating in the formation of an oligomer, the generated linear oligomers will have the formula $C_{2n+2m}H_{4n+6m-2(n+m-1)}O_{3n+4m-(n+m-1)}$, where the terms -2(n+m-1) and -(n+m-1) in the hydrogen and oxygen atom stoichiometry indicate water loss from the oligomerization process. For ring oligomers, formulas characterised by the stoichiometry $C_{2n+2m}H_{4n+6m-2(n+m)}O_{3n+4m-(n+m)}$ are searched. Similarly, formulas resulting from the condensation of hydrated forms with the listed organic acids are calculated and researched.

2.2.3.5. X-ray photoelectron spectrometry (XPS)

https://doi.org/10.5194/egusphere-2024-4073
Preprint. Discussion started: 27 January 2025

X-ray photoelectron spectrometry (XPS) is used to quantify the elemental O/C ratio of the particle surface to a depth less than 10 nm. Measurements are performed with a VG ES-CALAB 250 instrument using monochromatic Al K_α radiation (1486.6 eV). The O/C ratio is quantified by integrating the areas of O_{1s} and C_{1s} peaks. This last is contributed by a number of functions, including $–CO_2$, C–O, C–C/C–H as well as C-F from the Teflon substrate. The contribution of the latter can be evaluated from the F1s (approximately 690 eV) as described in Denjean et al., (2015). The contribution of SiO_2 from the mineralogical composition of the dust to O1s was evaluated by integrating the Si2p peak (107 eV) and applying the stoichiometric proportions between silicon and oxygen in the composition of quartz (O/Si = 2). The O/C_{surf} ratio is calculated as follows

$$O/C_{surf} = \frac{n[O_c]}{n[C]} = \frac{(n[O]-2n[Si])}{n[C]} \quad (3)$$

Where $n[O_c]$ is the signal coming from oxygen bonded to carbon atoms only, $n[C]$ is the signal of C_{1s}, $n[O]$ the area from O_{1s} and n[Si] is the area of the signal from Si_{2p} that is multiplied by 2 to take into account the silica stoichiometry. The XPS measurement on a filter collected during one ageing experiment are shown as an example in Figure S1 in the Supplementary Material.

2.3 Calculation of the glyoxal uptake coefficient

The uptake coefficient γ is defined as the probability of the gas to be taken up on the aerosol surface. It is a unit-less parameter expressed by the ratio between the number of molecules taken up on a surface and the total number of collisions of the gas on the surface as

$$\gamma = \frac{number\ of\ total\ molecules\ taken\ up}{total\ number\ of\ collisions} \quad (4)$$

The uptake coefficient γ can be calculated in two ways. First of all, it can be estimated from the first-order heterogeneous loss rate of glyoxal (k_{het}, s^{-1}) as

$$\gamma = \frac{k_{het}}{\omega} \quad (5)$$

https://doi.org/10.5194/egusphere-2024-4073
Preprint. Discussion started: 27 January 2025

where ω is the rate of collisions (collision frequency) defined as

$$\omega = \frac{cA_S}{4} \tag{6}$$

where:

- $c = 146 \times \sqrt{\frac{T}{MW}}$ is the mean molecular speed (m s^{-1}), where T is the air temperature (here 298 K) and MW the molecular weight of the compound of interest (in the case of glyoxal MW = 58 g mol^{-1}).
- A_S is total aerosol surface concentration (m^2 m^{-3}).

The total aerosol surface concentration (A_S) is calculated from the aerosol size distribution recorded at the end of the dust injection.

The heterogeneous loss rate of glyoxal (k_{het}) due to its uptake on dust particles can be determined as the difference of the loss rate of glyoxal measured during the uptake experiments (k_{obs}) and the glyoxal loss rate on the chamber walls (k_{loss}) as

$$k_{het} = k_{obs} - k_{loss} \tag{7}$$

The glyoxal wall loss is represented by a partition equilibrium described by two first-order reactions: one for the adsorption of gas phase molecules onto the chamber walls, and one for the reverse process. The rate constants for both processes have been obtained experimentally through control experiments with only glyoxal in the chamber in different relative humidity conditions.

If the uptake reaction is of the first rate, k_{het} is henceforth calculated as

$$k_{het} = \frac{ln\left(\frac{[Gly]_0}{[Gly]_{obs}}\right) - ln\left(\frac{[Gly]_0}{[Gly]_{loss}}\right)}{t} \tag{8}$$

where $[Gly]_0$ is the initial concentration of glyoxal, $[Gly]_{obs}$ represents the observed evolution of glyoxal concentration in time, resulting from the sum of uptake and wall

https://doi.org/10.5194/egusphere-2024-4073
Preprint. Discussion started: 27 January 2025

loss, and $[Gly]_{loss}$ represents the estimated glyoxal concentration resulting from the wall loss.

In addition, $k_{F\text{-}OM}$, the rate of formation of the particulate organic matter (POM) on pre-existing particles following the uptake of glyoxal on the dust can be calculated as

$$k_{F-OM} = \frac{ln\left(\frac{[POM]_t}{[POM]_0}\right)}{t} \quad (9)$$

where $[POM]_0$ represents the initial POM concentration in the particle phase, and $[POM]_t$ represents the concentration of the POM formed at a given time.

If the hypothesis that the POM formation is solely due to the uptake of glyoxal, γ can be also evaluated as

$$\gamma = \frac{k_{F\text{-}POM}}{\omega} \quad (10)$$

3 Results and discussion

3.1 Timeline of experiments

The ageing experiments of monodispersed mineral dust and glyoxal described in this paper are summarised in Table 1. All the aerosol data are corrected for dilution, wall loss, and particle loss through the tubing systems as detailed in Text S2 in the Supplementary Material. Gas phase concentrations are corrected for dilution only.

Table 1. Listing and initial conditions of the experiments considered in this study, including experiments with glyoxal only (experiment type GL), ammonium sulphate and glyoxal (AS + GL), dust only (D) and dust with glyoxal (D + GL). The glyoxal and ozone gas phase concentrations correspond to the maximum value measured by FTIR after the respective injections. V_{seed} indicates the maximum volume concentrations of seed particles (either dust or ammonium sulphate) measured after the particle injection. The notation "dark/light" indicates experiments when filter samples were collected both in the dark and with irradiation.

Experiment type	Reagents	Date	Experiment number	RH, %	Light	$[O_3]$, ppb_v	Temp, K	[GL], ppb_v	V_{seed}, μm^3 cm^{-3}
Control	GL	29/04/2021	G_1	< 5	dark	---	292	1130	---
		11/02/2022	G_2	77	light	1440	291	627	---
	AS+GL	21/02/2023	AS_1	38	dark	---	298	527	50.1
		23/02/2023a	AS_2	35	dark	---	298	516	48.3

https://doi.org/10.5194/egusphere-2024-4073
Preprint. Discussion started: 27 January 2025

		23/02/2023b	AS_3	32	light	---	298	445	64.8
		07/09/2023	AS_4	81	light	---	301	779	304.1
		08/09/2023	AS_5	83	light	---	300	430	161.2
	D	31/01/2022	D_1	< 5	dark/light	---	292	---	31.5
		03/02/2022	D_2	75%	dark/light	---	293	---	55.4
Uptake	D+GL	04/02/2022	D_3	< 5	dark/light	---	293	690	35.6
		08/02/2023	D_4	32	dark	---	294	940	21.5
		09/02/2023	D_5	31	light	---	295	1050	52.7
		10/02/2023	D_6	35	dark	---	294	809	37.4
		13/02/2023	D_7	34	light	---	296	850	51.3
		30/04/2021	D_8	76	light	---	289	759	28.3
		03/05/2021	D_9	79	light	---	290	607	38.7
		04/05/2021	D_{10}	81	light	---	290	371	31.5
		05/05/2021	D_{11}	78	dark	---	291	805	30.1
		06/05/2021	D_{12}	82	dark	---	292	432	21.1
		08/02/2022	D_{13}	81	dark/light	1270	293	555	64.0
		09/02/2022	D_{14}	78	dark/light	1450	293	756	79.8
		10/02/2022	D_{15}	75	dark/light	---	295	600	68.4
		14/02/2023	D_{16}	83	dark	---	296	661	35.8
		15/02/2023	D_{17}	75	light	---	298	444	41.0

Table 1 also lists the few control experiments using ammonium sulphate as seed particles, described in detail in Text S3 in the Supplementary Material. No POM formation is observed during control experiments with dust or glyoxal only, both dry and humid conditions and with and without irradiation.

The typical timelines of the particle concentrations (number and volume) and the non-refractory composition measured in dry conditions and at 30% and 80% relative humidity are shown in Figure 1.

https://doi.org/10.5194/egusphere-2024-4073
Preprint. Discussion started: 27 January 2025

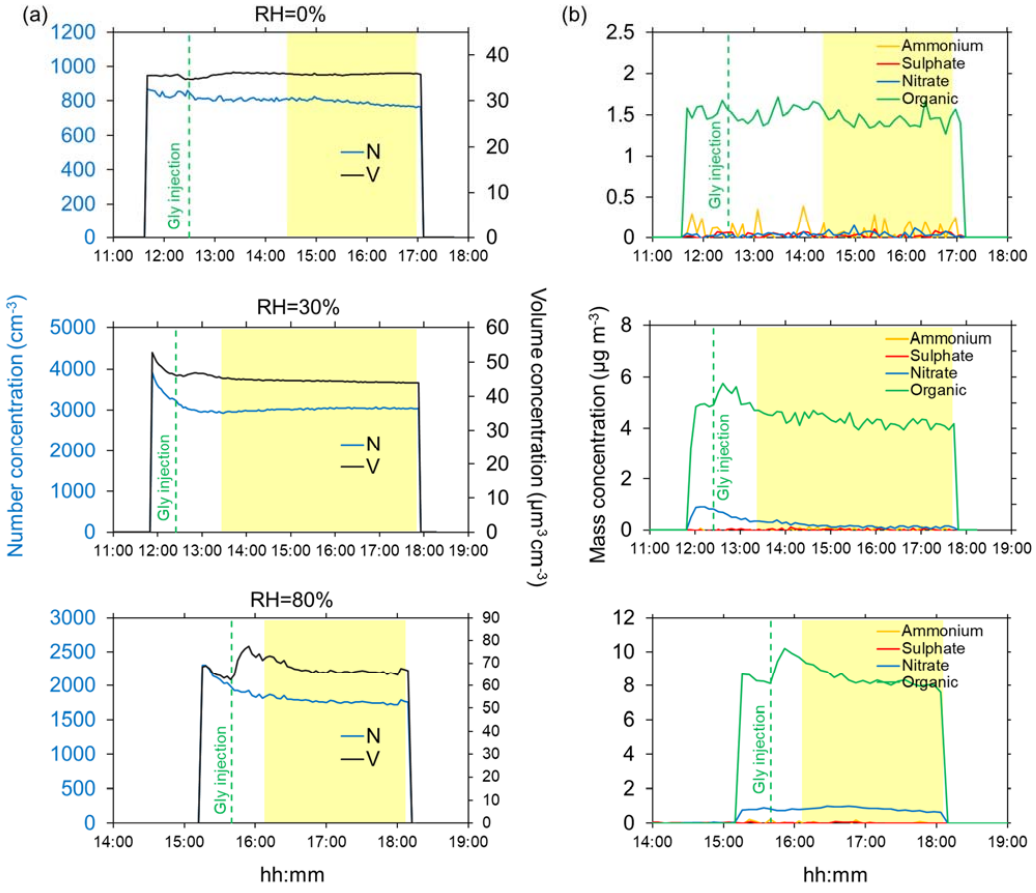

Figure 1. Timeline of ageing experiments of submicron dust with gas-phase glyoxal in dry conditions (top, experiment D_3), 30% (middle, experiment D_7), and 80% RH (bottom, experiment D_{15}). Left (a): aerosol total number (N) and volume (V) concentrations (blue and black lines, respectively) calculated from the measured dust size distributions. Right (b): mass concentrations of ammonium, sulphate, nitrate and organic (yellow, red, blue and green lines, respectively) measured by the ACSM. The yellow-highlighted portion of the graph indicates the interval where irradiation takes place, while the green vertical dashed lines indicate the injection glyoxal in the chamber. The dust injection corresponds to the time of the initial increase of the number and volume concentrations. Aerosol time series are corrected for dilution, wall loss and particle loss through the tubings.

Figure 1 shows that in dry conditions, there is no significant variation of either the aerosol number or the volume concentrations, nor the chemical composition (including organics) following the glyoxal injection.

At 30% RH, a small increase in the total volume concentration (approximately 5 μm^3 cm^{-3}) is observed for about 30 minutes after the injection of glyoxal. This corresponds to an increase of the POM of about 1 $\mu g\ m^{-3}$, approximately 20% more with respect to

https://doi.org/10.5194/egusphere-2024-4073
Preprint. Discussion started: 27 January 2025

the value measured before the uptake. On the other hand, the particle number concentration shows an apparent decrease at the beginning of the experiments, possibly because the particle loss correction model of Lai and Nazaroff (2000) does not fully apply to dust particles and humid conditions (see discussion in Battaglia et al. (2024). After that, and through the duration of the experiment, however, it remains constant, indicating that the increase in the particle volume occurs on the dust particles and not because of new particle formation.

At 80% RH, the increase in both the total volume and the POM concentrations is more pronounced, approximately 10-15 $\mu m^3\ cm^{-3}$ and 2 $\mu g\ m^{-3}$, respectively. As for 30% RH, both total particle volume and the POM concentrations return to values observed prior the injection of glyoxal, within approximately 30 minutes from their maximum values, likely due to evaporation. A similar behaviour is observed in the presence of ozone (not shown). As for 30% RH, the particle number concentration slightly decreases in time at the beginning of the experiment, but then remains constant, again excluding the formation of new particles but rather confirming the formation of organic matter on pre-existing particles. This is also supported by the fact that the rate of increase of POM and particle volume is the same (slope 3.2 $10^{-4}\ s^{-1}$ and 3.2 $10^{-4}\ s^{-1}$, respectively for POM and total volume), as shown by Figure S2 in the Supplementary Material.

On the other hand, the ratio between the observed increase of the POM (2 $\mu g\ m^{-3}$) and that of the particle volume concentration (20 $\mu m^3\ cm^{-3}$) corresponds to an estimated mass density of the order of 0.1 $g\ cm^{-3}$, that is, about 10 times lower than the value of 1 $g\ cm^{-3}$ expected for glyoxal. This would suggest that part of the organic matter formed on dust is not detected by the ACSM, as will be further demonstrated in section 3.3. On the other hand, Figure S2 shows that, after reaching its maximum value, the volume concentration decreases at a lower rate than the POM (slope 3.9 $10^{-5}\ s^{-1}$ and 6.1 $10^{-5}\ s^{-1}$, respectively). This suggests that an additional process could contribute the particle volume concentration partially compensating the loss of organic matter on the dust particles.

This is confirmed by Figure 2 comparing the variation in time of the particle volume distributions, normalised to the total volume, at four different times of the experiments at 30% and the one at 80%: prior and when the glyoxal is injected, when the POM reaches its peak value, and at the end of the experiment.

https://doi.org/10.5194/egusphere-2024-4073
Preprint. Discussion started: 27 January 2025

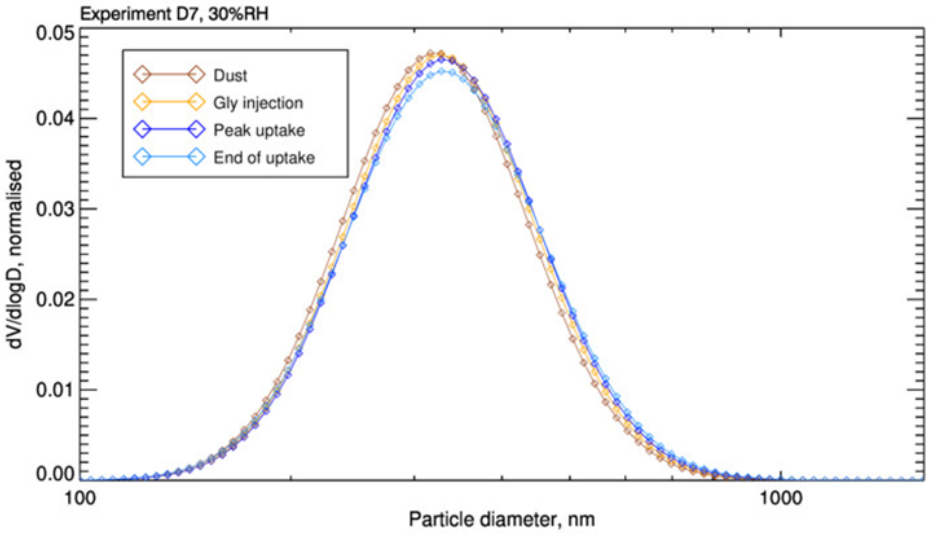

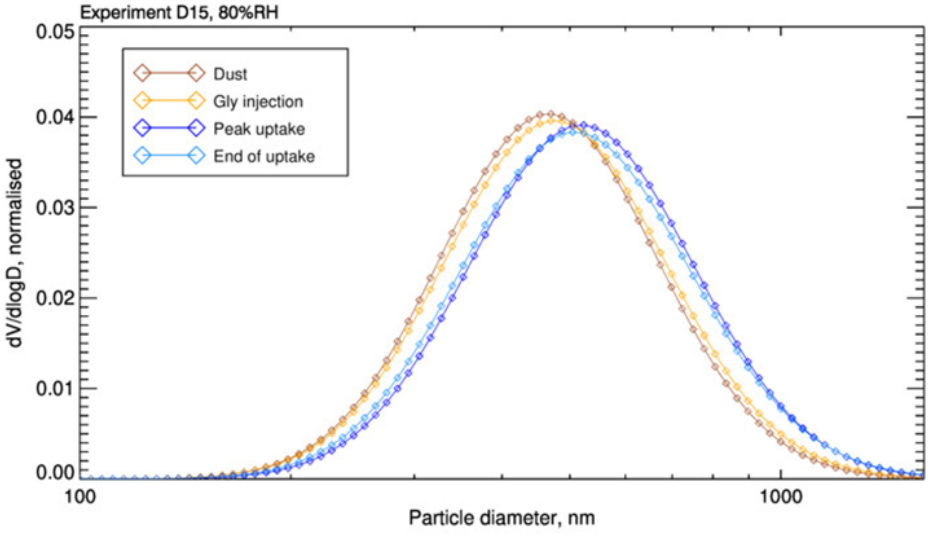

Figure 2. Evolution of volume-size distributions for two glyoxal uptake experiments in different relative humidity conditions. The images illustrate the progression of volume-size distributions recorded at four key moments during the experiments. The first distribution (orange) is recorded after the dust is injected into the simulation chamber. The second distribution (yellow) is recorded at the moment of glyoxal injection. The third distribution (blue) corresponds to the peak uptake of glyoxal on the aerosol, and the fourth (light blue) is recorded at the end of glyoxal uptake process. The left image depicts the evolution for the experiment D7 conducted at 30% RH, while the image on the right shows the distributions for the experiment D15 conducted at 80% RH. The results highlight that the distributions grow more significantly at 80% RH, indicating a higher glyoxal uptake and organic formation at elevated humidity levels.

All distributions have a single mode. However, after the injection of glyoxal, the geometric mean volume diameter, measured at the maximum POM concentration,

https://doi.org/10.5194/egusphere-2024-4073
Preprint. Discussion started: 27 January 2025

increases by up to 10% (from 310 to 340 nm) at 30% RH, and up to 20% (from 450 to 540 nm) at 80% RH. Interestingly, even at the end of the experiment, when the POM concentration returns to its initial value, the increase in geometric mean diameter of the aerosol is irreversible. This effect could be explained by the hypothesis that the uptake of glyoxal enhances the dust hygroscopicity. After glyoxal uptake, the particle becomes more hygroscopic and the difference in total volume between the beginning and end of the experiment is due to water uptake which adds up to the formed organic aerosol mass.

Finally, Figure 1 shows also that, while sulphate and ammonium are never detected, a background concentration of nitrate up to 1 μg m^{-3} is measured by the ACSM as soon as the dust particles are injected in the presence of water. We attribute it to the heterogeneous interaction between NO_2 and the dust particles (Goodman et al., 1999) as indeed, a background concentration of a few ppb of NO_2 is present in the chamber as a result of the procedure used to reduce the TOC content in the injected water (see Figure S3 in the Supplementary Material). However, since the contribution of nitrate represents at maximum 1% of the injected dust mass and whether decreases or remains constant throughout the experiment, its contribution to the particle growth and overall ageing of the mineral dust should be negligible.

Figure 3 shows the time series of the gas-phase compounds detected during the same experiment (D_{15}) at 80% RH.

https://doi.org/10.5194/egusphere-2024-4073
Preprint. Discussion started: 27 January 2025

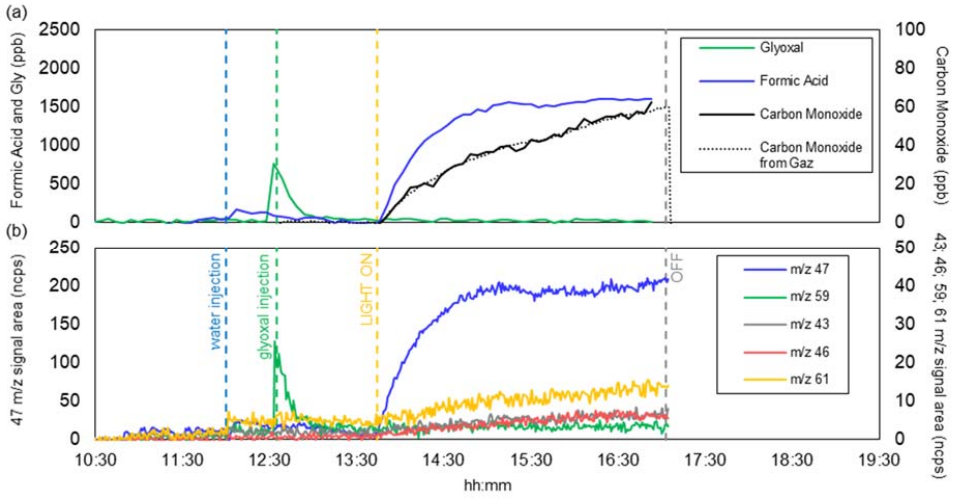

Figure 3. Time series of the gas-phase composition observed during experiment D_{15}: (a) concentrations of carbon monoxide, glyoxal and formic acid measured by FTIR (for CO the measured of the online analyser are also shown); (b) various VOC ions (m/z 47, 59, 43, 46 and 61) measured by the PTR-MS. Ion signals measured by PTR-MS are normalized by signals of reagent ions (i.e. H_3O^+ and $H_3O^+(H_2O)$) and therefore expressed in normalized counts (ncps). The blue vertical dashed lines indicate the injection of water in the chamber; the green vertical dashed lines indicate the injection of glyoxal in the chamber, the yellow dashed lines indicate the beginning of irradiation and the grey dashed lines indicate the end of irradiation.

The measured glyoxal concentration after the injection (Figure 3a) is lower than the nominal concentration of 1 ppm and goes to zero within minutes due to the rapid interactions with the walls of the chamber, water vapour, and the dust particles. Upon irradiation, formic acid and carbon monoxide are formed, as expected by the photolysis of glyoxal (De Haan et al., 2020). Fragments m/z = 46 and 47 are observed during water injection and photolysis, and could originate from the deprotonated and protonated form of formic acid, respectively. This suggests that a minor fraction of the formic acid could result from the desorption of compounds (including glyoxal) from the chamber walls. Fragments m/z = 43 and m/z = 61, and occasionally m/z = 45 (not seen during experiment D_{15} and therefore not shown in Figure 3b), are observed at a normalised intensity two orders of magnitude lower than that of formic acid, but not attributed. The quantification with both PTR-MS and FTIR in our experimental RH conditions is complicated by the presence of water, which reduces the sensitivity of PTR-MS and can interfere with the absorption of various organic compounds, making their quantification less accurate.

https://doi.org/10.5194/egusphere-2024-4073
Preprint. Discussion started: 27 January 2025

3.2 Glyoxal uptake coefficient

For experiment D_{15} at 80% RH, Figure 4 shows the temporal evolution of the natural logarithm of the glyoxal concentration measured by the FTIR, compared to that measured during a typical blank experiment without dust particles. Figure 4 additionally shows the variation of the aerosol organic fraction measured by the ACSM during the same time period.

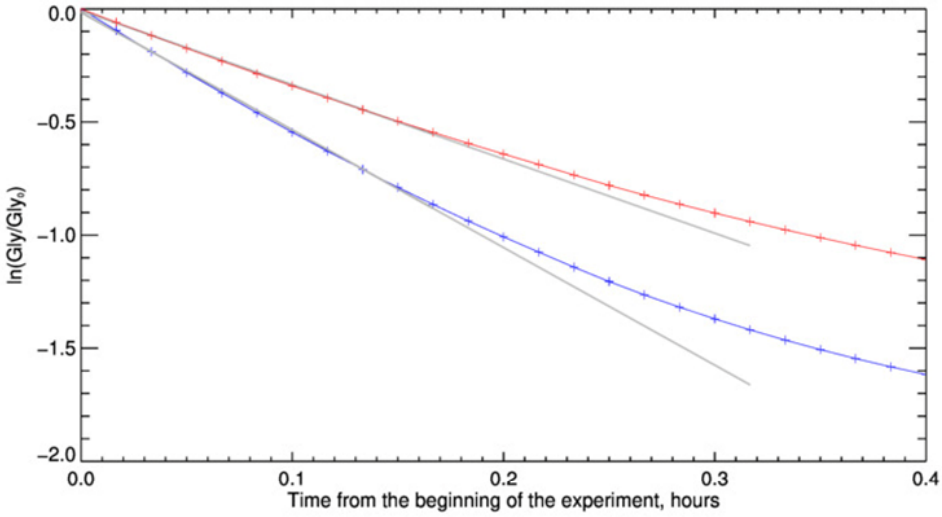

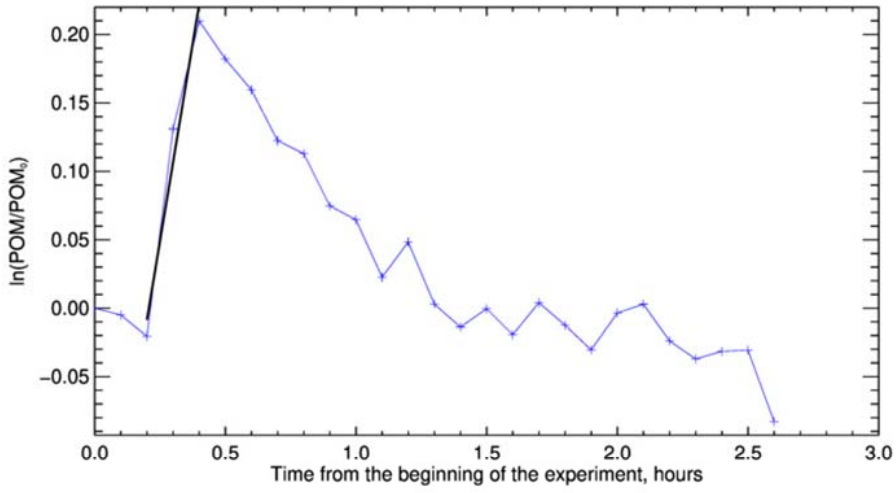

Figure 4. Measurement of glyoxal uptake coefficient on dust for the experiment D_{15}, conducted at 80% RH. The figure compares the two methods for measuring the uptake coefficient. In the top image, results are shown for the method based on monitoring the decay of gas-phase glyoxal. The red and blue curves

https://doi.org/10.5194/egusphere-2024-4073
Preprint. Discussion started: 27 January 2025

represent the logarithm of the ratio between the calculated decay of gas-phase glyoxal in the absence and presence of dust aerosols, respectively. The black lines represent the linear fit whose slope provides the heterogeneous kinetic constants of the two processes. The image at the bottom displays the result of the uptake coefficient measurement for the same experiment, obtained from the organic formation on the aerosol monitored by ACSM. The blue time series shows the logarithm of the ratio between the measured organic concentration divided by the initial organic on dust aerosol, while the black line is the linear fit representing the kinetics of organic formation.

Within the first 10 minutes after the injection of glyoxal, the decrease of the natural logarithm concentrations ratio with time in the presence of dust is linear (the rate is constant). After that, the loss slightly deviates from linearity. The difference from linearity is more evident for the blank experiment, when it occurs earlier than when the dust is present. These observations indicate that, within the first 10 minutes, the uptake of glyoxal on the dust particles can be considered to follow a first-order kinetic and its rate represents an initial uptake coefficient. In the following 20 minutes approximately, the uptake slows down, possibly because all the sites available on the particle surface become occupied, but also because that desorption from the particle surface could reinject glyoxal in the reactive mixture. On the particle phase, the natural logarithm of the organic concentration, normalised by its initial value increases rapidly and linearly, almost on the same time scale of that of the loss of glyoxal, but then decreases to return to its initial value within approximately one hour. These observations confirm that the uptake of glyoxal results in a formation of OA on the dust particles, but that this process is reversible.

The uptake coefficients calculated as the linear fit of the glyoxal and particle organic concentration are presented in Table 2.

Table 2. Uptake coefficients for glyoxal on mineral dust and ammonium sulphate calculated from the loss of gas-phase glyoxal and the rate of OA formation for the experiments conducted at 80% RH. The initial glyoxal concentration is reported. The aerosol surface concentration (A_s) corresponds to the value preceding the glyoxal injection. Ozone concentration is the maximum concentration measured by FTIR spectroscopy after the injection. For ammonium sulphate, only the γ values calculated from the loss of gas phase glyoxal are presented, as the ACSM collection efficiency (CE) for ammonium sulphate varies significantly during OA formation (Matthew et al., 2008).

Date	Experiment ID	RH%	$[GL]_0$, ppb_v	Ozone (ppb)	A_S (m^2 m^{-3})	ω (s^{-1})	γ_{gas}	$\gamma_{OA\ glyxoal}$
30/04/2021	D_8	76	759	---	$4.8\ 10^{-4}$	$3.9\ 10^{-2}$	$6.0\ 10^{-3}$	$1.0\ 10^{-3}$
03/05/2021	D_9	79	607	---	$6.1\ 10^{-4}$	$5.0\ 10^{-2}$	$1.5\ 10^{-2}$	$1.5\ 10^{-2}$
04/05/2021	D_{10}	81	371	---	$5.1\ 10^{-4}$	$4.2\ 10^{-2}$	$1.7\ 10^{-2}$	$9.0\ 10^{-3}$
05/05/2021	D_{11}	78	805	---	$4.6\ 10^{-4}$	$3.8\ 10^{-2}$	$8.0\ 10^{-3}$	$5.0\ 10^{-3}$
06/05/2021	D_{12}	82	432	---	$3.5\ 10^{-4}$	$2.9\ 10^{-2}$	$1.2\ 10^{-2}$	$2.3\ 10^{-2}$
08/02/2022	D_{13}	81	555	1270	$7.1\ 10^{-4}$	$5.8\ 10^{-2}$	$4.0\ 10^{-3}$	$4.0\ 10^{-3}$
09/02/2022	D_{14}	78	756	1450	$8.5\ 10^{-4}$	$7.0\ 10^{-2}$	$4.0\ 10^{-3}$	$5.0\ 10^{-3}$
10/02/2022	D_{15}	75	600	---	$8.4\ 10^{-4}$	$6.9\ 10^{-2}$	$1.0\ 10^{-2}$	$5.0\ 10^{-3}$

https://doi.org/10.5194/egusphere-2024-4073
Preprint. Discussion started: 27 January 2025

14/02/2023	D_{16}	83	661	---	$6.0\ 10^{-4}$	$4.9\ 10^{-2}$	$4.0\ 10^{-3}$	$1.5\ 10^{-2}$
07/09/2023	AS_4	81	779	---	$6.3\ 10^{-3}$	$5.2\ 10^{-1}$	$9.8\ 10^{-4}$	---
08/09/2023	AS_5	83	430	---	$2.0\ 10^{-3}$	$1.7\ 10^{-1}$	$1.2\ 10^{-3}$	---
Average dust							$9\ (\pm\ 5)\ 10^{-3}$	$9\ (\pm\ 7)\ 10^{-3}$
Average AS							$1.1\ (\pm\ 0.2)\ 10^{-4}$	

The average uptake coefficients for glyoxal on the Gobi mineral dust calculated at 80% RH from the gas-phase uptake and the particle formation are $\gamma_{Gly\text{-}Dust\text{-}gas} = 9 \times 10^{-3}$ (standard deviation ± 5) and $\gamma_{Gly\text{-}Dust\text{-}OA} = 9 \times 10^{-3}$ (standard deviation ± 7), respectively. The two average values agree. This suggests that every glyoxal molecule in the gas phase is taken up by the airborne dust particles. This suggests also that the uptake occurs on airborne particles only, as expected as the dust particles are selected in the submicron range and that minimal deposition of dust particles is observed in the first 30 minutes after injection. The primary mechanism of particle loss during this period is dilution, which does not interfere with uptake. The standard deviations of the mean values are large, being attributed to the fact that the state of the chamber walls and the dust size distribution vary from one experiment to the other, and that the aerosol/chamber walls surface ratio is very low (0.08-1.5 10^{-3}). The presence of ozone appears uninfluential.

The results of the current study can be compared with the literature. Shen et al. (2016) investigated the uptake of glyoxal on mineral proxies, i.e. SO_2 and $CaCO_3$ under various levels of relative humidity. These authors determined the uptake coefficients after a long exposition of the surface to glyoxal (steady state uptakes) and found that the uptake coefficients are reduced with increasing the gas phase concentration of glyoxal. At 1 ppb concentration and a relative humidity of 60% the uptake coefficients determined on suspended particles of calcite ($CaCO_3$, $\gamma = (1.4 \pm 0.1) \times 10^{-4}$) and alumina ($AlO_3$, $\gamma = (5.5 \pm 0.1) \times 10^{-5}$). Our values are measured in a shorter time frame and correspond to an initial uptake of glyoxal. They are approximately one order of magnitude higher than those obtained by Shen et al. (2016). These authors scaled the uptake coefficient to the specific surface area of the dust, which henceforth could correspond to a lower limit. On the contrary, in our case, we use a geometric surface area (assuming spherical particles) which could lead to an overestimation of the uptake coefficient.

https://doi.org/10.5194/egusphere-2024-4073
Preprint. Discussion started: 27 January 2025

Zogka et al. (2024) used a Knudsen cell to evaluate the initial and steady state glyoxal uptake coefficient bulk soil samples of various origins. At low relative humidity, these authors found that for Gobi soil sieved to less than 63 µm in diameter the initial uptake coefficient using the geometric surface area was 0.18 (corresponding to an upper limit of the uptake) independent of glyoxal concentration. However, the steady state uptake coefficients determined after a long processing of surface were found to decrease with increasing glyoxal concentration, due to aging of the surface.

Various reasons can explain these apparently different results. First of all, in CESAM we measure the initial uptake coefficient at humid conditions, which is independent of concentration. On the other hand, Shen et al. (2016) measured steady-state uptake coefficient at lower glyoxal concentrations (< 1 ppb) than we did (>400 ppb). As shown by both Shen et al. (2016) and Zogka et al. (2024), the steady-state uptake coefficient decreases with the concentration of glyoxal, regardless of the relative humidity.

Secondly, the uptake coefficient is inversely proportional to the available particle surface, which in our case is smaller than Zogka et al. (2024) who used soils sieved to 63 µm. Shen et al (2016) used standard mineral particles of various sizes from 35 nm to 5 µm, while our particle size distribution peaked between 300 and 400 nm. Shen et al. (2016) used single minerals, while Zogka et al. (2024) and our study share the same soil sample from Gobi. While the uptake coefficient should depend on the dust mineralogy, this is difficult to ascertain in the present study.

Overall, although the experiments performed in literature with those of the current study were performed under different conditions, results indicate that natural Gobi dust is an effective sink of glyoxal, with initial uptake coefficient independent of glyoxal concentration, pointing to a first order removal process. However, the long-term ageing of particles leads to lower uptake coefficients that strongly depend on glyoxal concentration due to the depletion of surface sites.

3.3. Organic composition

This section discusses the chemical composition of the organic matter on mineral dust following the interaction with glyoxal. Details on the organic composition of the native dust are provided in Text S4 in the supplementary material.

https://doi.org/10.5194/egusphere-2024-4073
Preprint. Discussion started: 27 January 2025

3.3.1. Measurements by the ACSM

Figure 5 shows the time evolution of the intensity of the organic fragments detected by the ACSM at 80% RH (experiment D_{15}) before the injection of glyoxal (dust only), during the POM formation, after the maximum concentration, and at the end of the experiment, when it returned to its initial value.

https://doi.org/10.5194/egusphere-2024-4073
Preprint. Discussion started: 27 January 2025

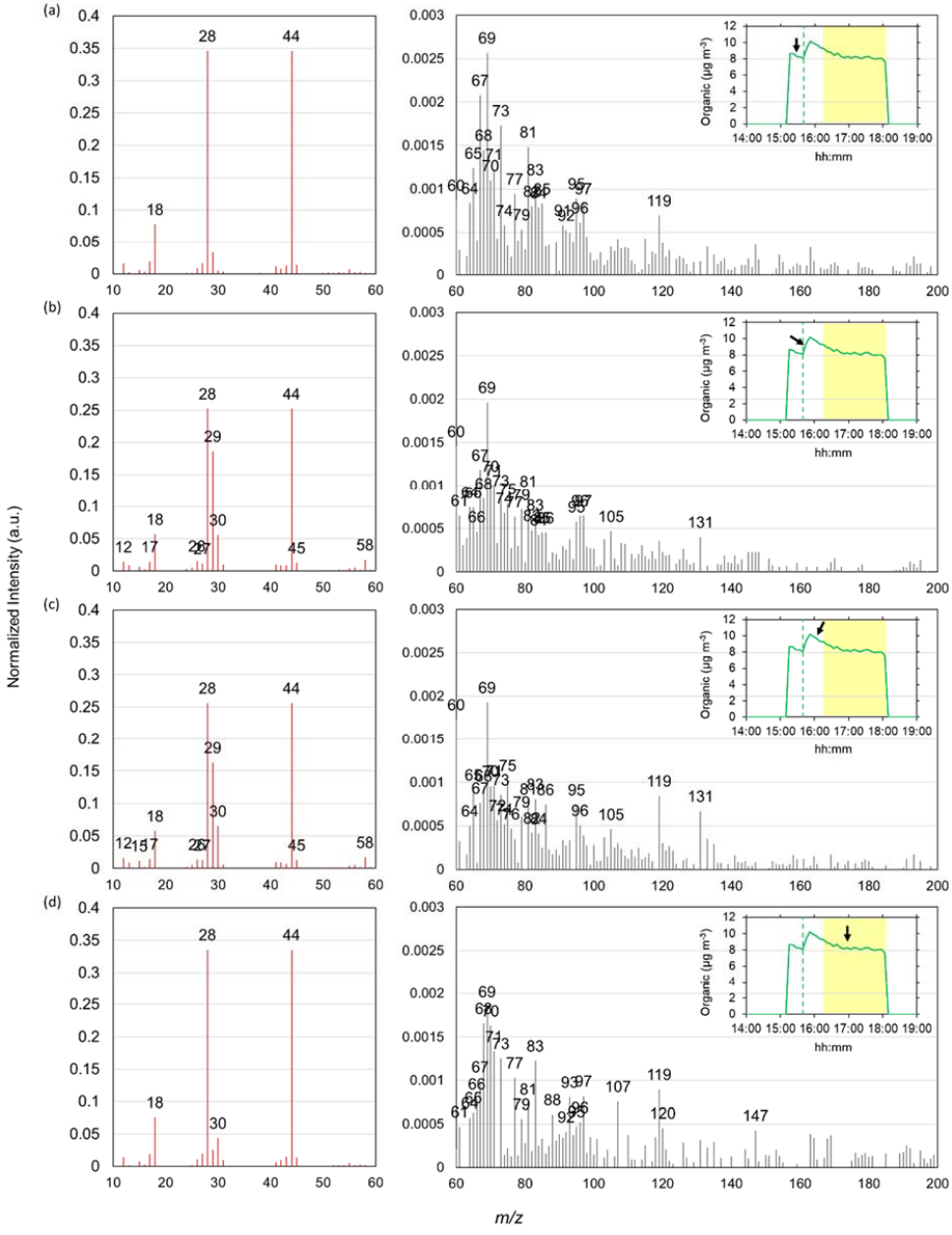

Figure 5. ACSM organic mass spectra (intensities normalized to the total organic concentration) recorded during the experiment D_{15}: (a) before glyoxal uptake (dust organic fraction composition), (b) during glyoxal uptake, (c) after reaching the maximum uptake on the particles and (d) 1h later under irradiation. Panels on the left show the mass spectra ranging from 10 to 60 m/z, while the panels on the right represent fragments from 60 to 200 m/z (their intensity is approximately one hundred times lower). The inserts display the time series of organic concentrations measured by the ACSM. A black arrow indicates the time corresponding to the mass spectrum shown. The yellow-highlighted shaded area indicates the interval where irradiation takes place, while the green vertical dashed lines indicate the moment of glyoxal injection in the chamber.

https://doi.org/10.5194/egusphere-2024-4073
Preprint. Discussion started: 27 January 2025

Fragments at 28 m/z and 44 m/z, typical of oxidised compounds, are ubiquitous at all stages of the experiment. Their relative intensity follows the kinetic of the uptake, decreasing during the formation of organic aerosols and reverting to their initial value towards the end of the experiments. Fragment 69 m/z, attributed to $C_3HO_2^+$ and $C_4H_5O^+$, has the highest intensity among ions above m/z 60 in all four spectra, suggesting that it is not related to glyoxal reactivity. Galloway et al. (2009) observed this fragment and identified it as a nitrogen-containing organic molecule with a formula $C_3H_3NO^+$ from the reaction of glyoxal with ammonia during the uptake of glyoxal on ammonium sulphate. This fragment was also observed at significant intensities in organic aerosols originating from phenolic derivatives, such as guaiacol and syringic acid, metabolites of plants (Sun et al., 2010), and could be explained as soil residues from vegetation but also animals (Nieder et al., 2018).

The signal of fragments at 29 m/z (CHO^+), 30 m/z (CH_2O^+), and 58 m/z (molecular peak $C_2H_2O_2^+$), characteristics of glyoxal, appear during the uptake (second panel from the top in Figure 5) but their relative intensity decreases with time. Fragments m/z = 105 and m/z = 131 observed during both the uptake and the photolysis are specific markers of the interaction between dust and glyoxal (Liggio et al., 2005). The former is attributed to an oligomeric structure of glyoxal generated by the condensation of two molecules of glyoxal hydrate (see also Table 3 in Liggio et al. (2005)). The latter is not identified, yet it consistently accompanies the glyoxal's primary ions. In photo-oxidation experiments of glyoxal in the aqueous phase, Carlton et al. (2007) found that its abundance increased proportionally with the increase in glyoxal concentration. In our study, this fragment is detected in all conditions (with and without light or ozone).

Fragments at 119 and 120 m/z have been observed in organic aerosols derived from isoprene and attributed to an organic acid with the formula $C_8H_8O_4$ (m/z 120) and its deprotonated form (Safi Shalamzari et al., 2013). In our experiments, they consistently increase after glyoxal uptake, and in particular upon irradiation. Although it is not straightforward to assign these fragments to a unique glyoxal derived formula, we hypothesise that they may arise from oxidised forms of oligomers.

Upon irradiation, m/z = 147 is accompanied by m/z = 165. These fragments have been observed in organic aerosols produced in experiments of aqueous phase glyoxal oxidation via OH radicals (Lim et al., 2010). The fragment m/z 165 is attributed to the

https://doi.org/10.5194/egusphere-2024-4073
Preprint. Discussion started: 27 January 2025

condensation of one molecule of glyoxal di-hydrate with one molecule of oxalic acid or two molecules of glyoxylic acid hydrate. The fragment m/z 147 could result from the dehydration of the aforementioned products. These fragments are present with similar intensity in the spectrum of native dust, and their increase in intensity under irradiated conditions might therefore be due to the reversibility of the interaction rather than an oxidation process of glyoxal.

The occurrence of the fragment at 18 m/z is often resulting from the loss of a water molecule (H_2O) from hydrated organic compounds. The slight decrease of the intensity of this fragment during glyoxal uptake could therefore be explained by the presence of the oligomerization of hydrated glyoxal molecules. This process leads to the loss of two hydroxide groups for each added molecule in favour of the formation of acetal or hemiacetal bonds in the structure of the resulting newly formed secondary organic aerosol.

3.3.2. Molecular analysis

The list and conditions of the samples analysed by SFE/GC-MS and ESI-Orbitrap are reported in Table S2 in the Supplementary Material. The summary of the organic molecules detected by those analysis is presented in Table 3 and discussed in the next paragraphs.

Table 3. *Summary of frequently observed compounds identified by SFE/GC-MS analysis and glyoxal-related formulas observed with ESI-Orbitrap, along with the suggested structures under the different experimental conditions tested.*

Molecular formula	Name	Tentative Structure	Technique	Experimental conditions
$C_2H_2O_3$	Glyoxylic acid	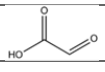	ESI-Orbitrap	Dust+Gly, 80%, Dark, O_3
$C_2H_4O_3$	Glycolic acid	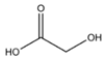	ESI-Orbitrap SFE/GC-MS	Dust+Gly, 30%, Dark Dust+Gly, 30%, Light Dust+Gly, 80%, Light Dust+Gly, 80%, Light, O_3
$C_2H_2O_4$	Oxalic acid	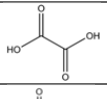	ESI-Orbitrap	Dust+Gly, 80%, Light
$C_2H_4O_4$	Glyoxylic acid monohydrate	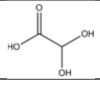	ESI-Orbitrap SFE/GC-MS	Dust+Gly, 80%, Light
$C_3H_6O_3$	Lactic acid		SFE/GC-MS	Dust, 80%, Light Dust+Gly, Dry, Dark Dust+Gly, 30%, Dark Dust+Gly, 30%, Light Dust+Gly, 80%, Light Dust+Gly, 80%, Dark, O_3 Dust+Gly, 80%, Light, O_3

https://doi.org/10.5194/egusphere-2024-4073
Preprint. Discussion started: 27 January 2025

$C_5H_8O_3$	Levulinic acid	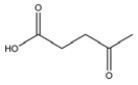	SFE/GC-MS	Dust, Dry, Dark Dust, 80%, Dark Dust, Dry, Light Dust+Gly, 30%, Dark Dust+Gly, 30%, Light Dust+Gly, 80%, Dark, O_3 Dust+Gly, 80%, Light, O_3
C_7H_8O	Benzyl alcohol		SFE/GC-MS	Dust, 80%, Dark Dust+Gly, 30%, Dark Dust+Gly, Dry, Light Dust+Gly, 30%, Light Dust+Gly, 80%, Light
$C_9H_{16}O$	Cyclohexanone, 3,3,5-trimethyl		SFE/GC-MS	Dust, 80%, Dark Dust+Gly, 30%, Dark Dust+Gly, 30%, Light Dust+Gly, 80%, Light, O_3
$C_4H_4O_4$	Glycolic acid dimer	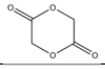	ESI-Orbitrap	Dust+Gly, 80%, Light
$C_4H_6O_5$	Glyoxal oligomer	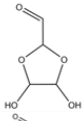	ESI-Orbitrap	Dust+Gly, 80%, Light
$C_6H_6O_6$	Glyoxal oligomer	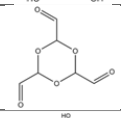	ESI-Orbitrap	Dust+Gly, 80%, Light
$C_8H_{16}O_{12}$	Glyoxal oligomer	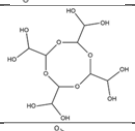	ESI-Orbitrap	Dust+Gly, 80%, Light
$C_{10}H_{12}O_{11}$	Glyoxal oligomer	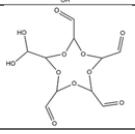	ESI-Orbitrap	Dust+Gly, 80%, Dark

3.3.2.1. SFE/GC-MS analysis

Figure 6 shows the comparison of four gas chromatograms obtained for experiments D_2, D_{13}, D_{15} and D_{16} at 80% RH, with and without irradiation, with and without ozone (Table 1).

https://doi.org/10.5194/egusphere-2024-4073
Preprint. Discussion started: 27 January 2025

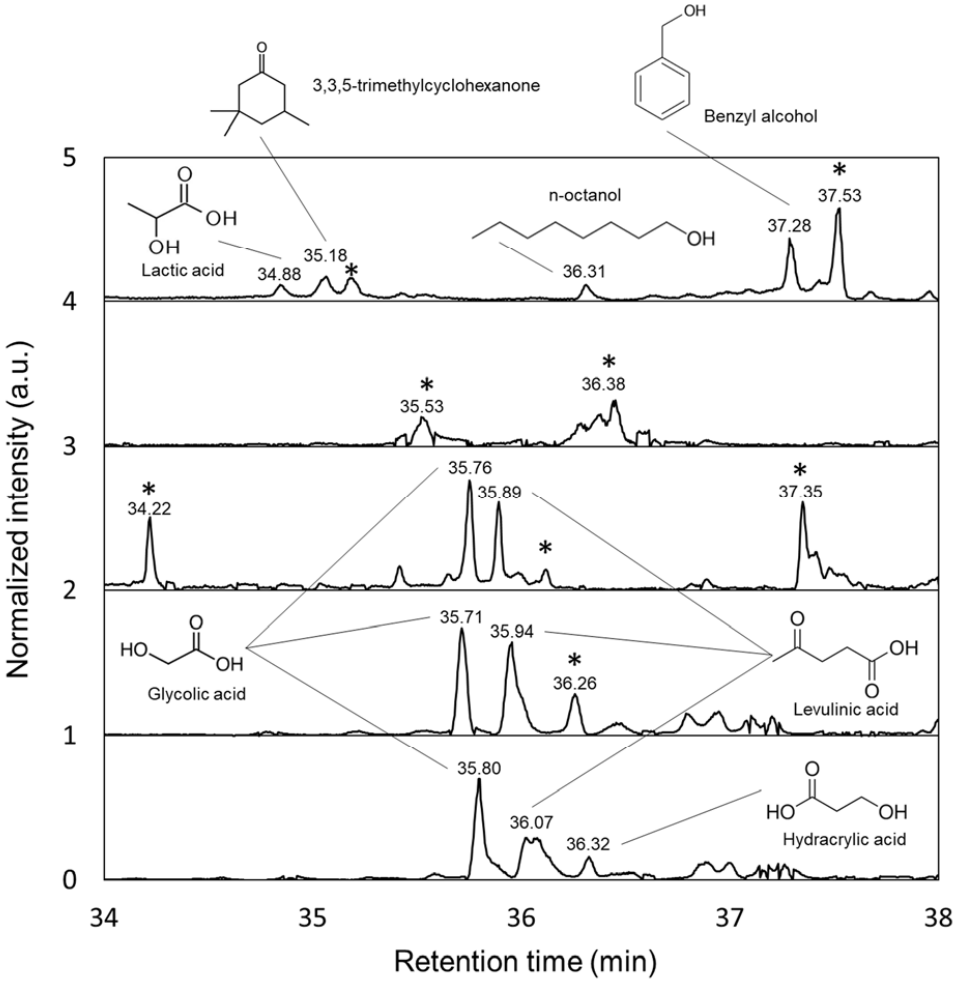

Figure 6. SFE/GC-MS chromatograms recorded from filters collected during one dust control experiment and four glyoxal uptake experiments under four different conditions. From up to bottom: the first chromatogram is from Experiment D_2, dust control experiment under 80% RH and irradiation. The second is from Experiment D_{16} with dust and glyoxal at 80% RH under dark conditions. The third is from Experiment D_{15} with dust and glyoxal at 80% RH under irradiated conditions. The fourth and fifth chromatograms are from Experiment D_{13} with dust and glyoxal at 80% RH in the presence of ozone under dark and irradiated conditions, respectively. The two peaks of higher intensity appearing after 41 minutes are from the internal standards added to the solution: tridecane around 41 minutes and ortho-toluic acid at about 41.8 minutes. The intensity is normalized to peak of the internal standard ortho-toluic acid. The chromatograms start at 32 minutes as 15 minutes are required for the removal of CO_2 from the extraction fluid, and approximately another 15 minutes represent the delay required for the solvent to pass through the column and reach the electron ionization (EI) MS detection. For the second and third spectra, is noticeable that under irradiated conditions the number of peaks increases significantly compared to dark conditions, likely due to enhanced chemical reactions driven by light. This effect appears to be less pronounced in the presence of ozone.

https://doi.org/10.5194/egusphere-2024-4073
Preprint. Discussion started: 27 January 2025

The chromatograms of samples collected in the presence of glyoxal generally exhibit a higher number of peaks compared to samples of dust-only, indicating glyoxal oxidation and production of organic aerosols. A higher number of peaks are detected in samples after irradiation compared to dark conditions (see Figure 6). This suggests that the exposure to light influences the chemical composition of the samples by promoting pathways that alter the chromatogram profile, possibly through photochemical reactions, which could lead to glyoxal oxidation products. However, in the presence of ozone and glyoxal, the chromatogram profile recorded under dark conditions is comparable to that recorded in the presence of light, suggesting that ozone may play a significant role in the oxidation process, driving similar chemical reactions in both light and dark environments. This could imply that the oxidative capacity of ozone is sufficient to promote glyoxal oxidation and organic formation independently of photolytic processes, resulting in comparable chromatogram profiles regardless of the presence of light.

The compounds identified using SFE/GC-MS primarily consist of carboxylic acids and relatively light-weight carbonyl compounds (<150 Da). Lactic and levulinic acids are detected in 10 and 9 samples, respectively, regardless of the experimental conditions. Compounds detected less frequently include benzyl alcohol, 3,3,5-trimethylcyclohexanone, methylphosphonic acid (5 samples), decanal (4 samples), and various organic acids, including heptanoic, propanedioic, and hydroacrylic acid (3 samples), as well as benzoic acid and 1-octanol (2 samples).

Glycolic acid and is only detected during experiments with glyoxal. Light and the presence of ozone seem to favour its formation. Indeed, the fourth panel in Figure 6 suggests that ozone might substitute light in promoting the formation of glycolic acid from glyoxal at high RH, suggesting an alternative oxidative pathway. Glycolic acid is also detected at 30% RH (not showed), both with and without light, in agreement with the experiments on dust by Shen et al. (2016), but differently than reported by Galloway et al. (2009) on ammonium sulphate. Monohydrated glyoxylic acid is found in one sample at 80% RH under irradiated conditions, likely due to the known pattern of oxidation of glyoxal and glycolic acid with OH radicals (Buxton et al., 1997).

Twelve mass spectra have a profile unrecognised by the NIST library. An example is shown in Figure 7.

https://doi.org/10.5194/egusphere-2024-4073
Preprint. Discussion started: 27 January 2025

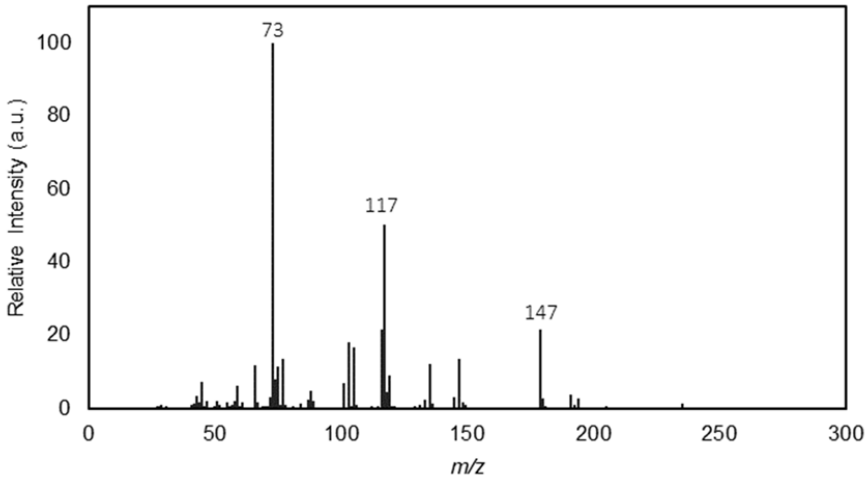

Figure 7. SFE Electron ionization mass spectrum recorded from the filter collected during the experiment D_{13} (80% relative humidity in the presence of O_3), where the characteristic peaks of the TMS functionalization of two hydroxyl groups (74 and 147 m/z) and one carboxylic group (117 m/z) are observed. The retention time of the peak corresponding to this mass spectrum was 39.58 min.

Notably, ten are collected under humid conditions (both 30% and 80% RH) and in the presence of light. Eleven are characterised by 73 m/z $[Si(CH_3)_3]^+$ for at least one functionalization, 147 m/z $[(CH_3)_2Si{=}OSi(CH_3)_3]^+$ for at least two, and their multiples for a greater number of hydroxyl functionalities (-OH). In addition, the fragment at 117 m/z $[COO{=}Si(CH_3)_3]^+$ is detected. These compounds are attributed to trimethylsilyl-multi-functionalised molecules from small oligomers of hydrated glyoxal (multiple functionalities) that have undergone partial oxidation, as indicated by the presence of carboxylic group peak in most of the spectra (117 m/z).

3.3.2.2. ESI-Orbitrap

On the 15 samples analysed by ESI-Orbitrap (Table S2 in the Supplementary Material), signals attributable to products of the oxidation, hydration, or oligomerization of glyoxal are found only for experiments at high relative humidity (80%), both in the dark but mostly in irradiated conditions. Figure 8 illustrates the mass spectrum and the assigned formula for experiment D_{10}.

https://doi.org/10.5194/egusphere-2024-4073
Preprint. Discussion started: 27 January 2025

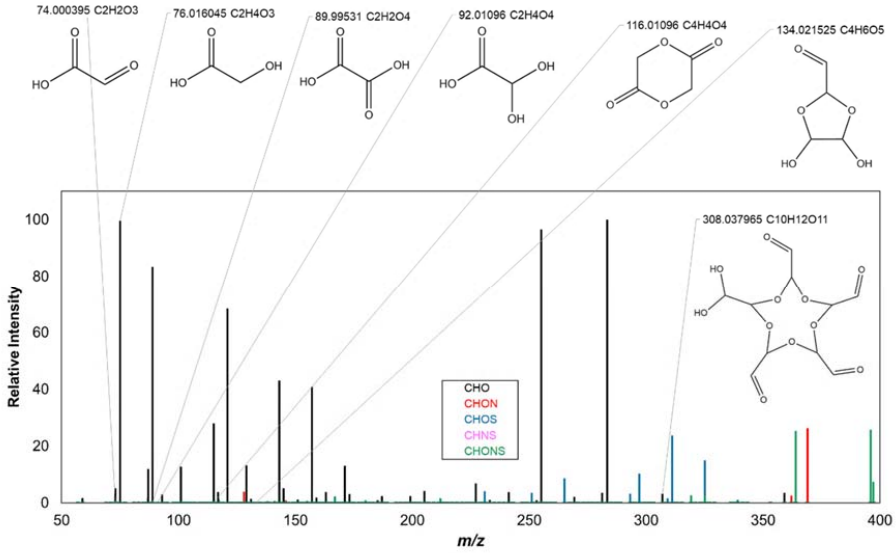

Figure 8. ESI Orbitrap MS from the filter D_{10}: uptake of glyoxal on mineral dust at 80% RH and under irradiation. In the mass spectra, the peaks referring to formulas for which is possible to suggest a structure from glyoxal reactivity are labelled.

Molecules corresponding to oxidised compounds are predominantly observed on filters collected under irradiated conditions: $C_2H_4O_3$ (also detected by SFE/GC-MS) attributed to glycolic acid; $C_2H_2O_4$, attributed to oxalic acid, and $C_4H_4O_4$, attributed to a dimer of glycolic acid. Its monohydrated form, $C_2H_4O_4$ (also detected by SFE/GC-MS) is also observed in dark conditions. In the presence of ozone, glyoxylic acid is also observed in dark conditions. Particle phase formic acid, observed on both dust and ammonium sulphate by various authors (Galloway et al., 2009; Rubasinghege et al., 2013; Shen et al., 2016), is not detected in our study neither by molecular analysis nor the ACSM. Although the reasons remain unclear, Shen et al. (2016) suggested that, above approximately 50% RH, adsorbed water could compete for surface reactive sites resulting in suppressing the formation of organic acids onto the dust particles. In contrast, the formation of glycolic and glyoxylic acid appears to be less affected by the presence of adsorbed water, as they are detected solely in humid conditions. This is possibly due to differences in their chemical pathways or their interactions with the dust surface. These acids may form through mechanisms that are less competitive with water adsorption, or their precursors have a higher affinity for the reactive sites on dust

https://doi.org/10.5194/egusphere-2024-4073
Preprint. Discussion started: 27 January 2025

particles (possibly due to the presence of two carbonyl regions) allowing their formation to proceed even in the presence of high humidity.

Compounds from C_4 to C_{10}, oligomerization products of the glyoxal mono and di hydrate forms, are observed only at 80% RH. The following peaks are detected and attributed: $C_4H_6O_6$ (1 monohydrated glyoxal + 1 dehydrated glyoxal forming a 5-atom ring), $C_8H_{16}O_{12}$ (4 dehydrated glyoxal molecules forming an 8-membered ring), and $C_{10}H_{12}O_{11}$ (4 monohydrated glyoxal molecules + 1 dehydrated glyoxal molecule forming a ring structure). The oligomer $C_6H_6O_6$ (3 molecules of monohydrated glyoxal forming a 6-membered ring) is detected only under dark conditions. $C_8H_{16}O_6$ corresponds to an oligomer previously observed by Shen et al. (2016) on mineral dust.

Based on the observations above, Figure 9 shows the suggested chemical mechanism.

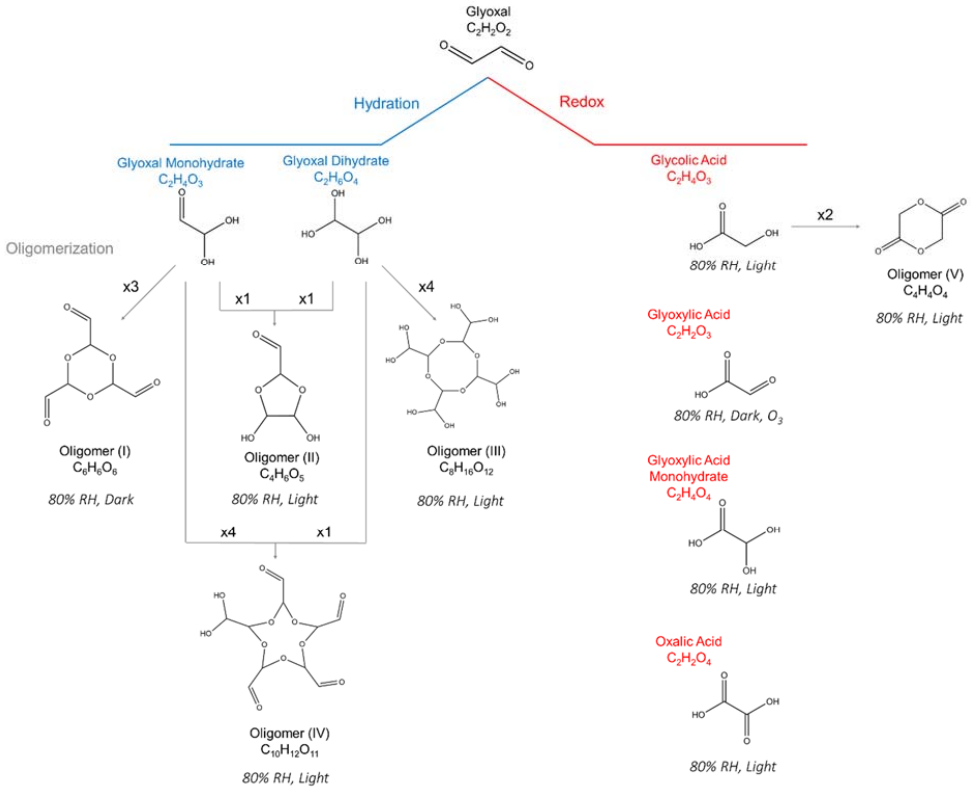

Figure 9. Proposed reaction scheme to explain the glyoxal-related molecular formulas detected through ESI-Orbitrap mass spectrometry and SFE/GC-MS.

https://doi.org/10.5194/egusphere-2024-4073
Preprint. Discussion started: 27 January 2025

The primary oligomers detected are attributed to the condensation of hydrated glyoxal forms specifically the mono- and di-hydrated glyoxal forms, through hydrolysis. The oligomer V is attributed to the condensation of two glycolic acid molecules.

3.4 Oxidation state and reversibility

The results on the oxidative properties of the aged dust are summarised in Figure 10 showing the van Krevelen diagram obtained from the ESI-Orbitrap analysis of a sample collected during experiment D_2 (dust control experiments without glyoxal) and a sample collected during experiment D_{10} (dust and glyoxal), both in the dark and with irradiation and 80% RH.

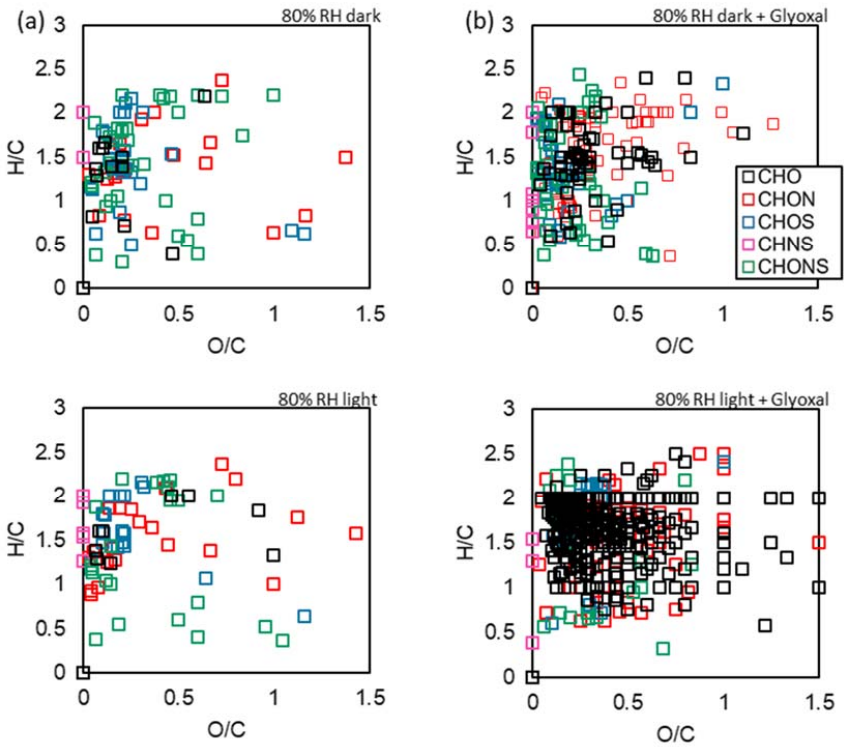

Figure 10. Van Krevelen diagrams recorded at 80% RH for: in the top line (a) experiments in the dark for mineral dust only (control experiment D_2, left) and one ageing experiment of dust with glyoxal (experiment D10); bottom line (b) same with irradiation.

Under the different conditions presented, the samples exhibited varying levels of particulate organic matter and number of ESI Orbitrap peaks detected.

https://doi.org/10.5194/egusphere-2024-4073
Preprint. Discussion started: 27 January 2025

In the absence of glyoxal, only a few signals are detected. In dark conditions, the particulate organic matter of filter is 0.9 µg with 102 peaks detected. In irradiated conditions, the particulate organic matter is 0.8 µg with 86 peaks detected. Peaks are mostly in the range of O/C < 1 and 0.5 < H/C < 2.5, both in the dark and with irradiation. The distribution of values of both ratios is rather similar, while the appearance of molecules for families CHON and CHONS is observed when the lights are on.

The number of detected signals increases significantly in the presence of glyoxal, (right column of Figure 10), in particular in the presence of light. In dark conditions, the particulate organic matter on the filter is 1.7 µg, yielding 398 signals detected. In irradiated conditions, the particulate organic matter is 0.6 µg, resulting in 310 signals detected. The predominant family in this case is that of CHO molecules. The appearance of signals with O/C ratio higher than 1 is attributed to photo-oxidation.

For comparison, the O/C ratio of the bulk aerosol measured at 80% RH by the ACSM and XPS is shown in Figure 11 (results in dry and 30% RH conditions are shown in Figure S4 in the Supplementary Material).

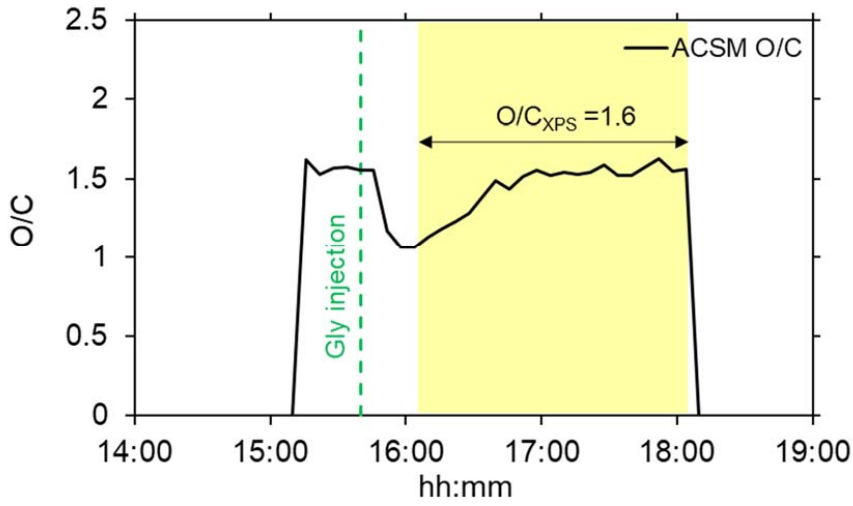

Figure 11. Time series of O/C ratio measured with the ACSM during ageing and 80% RH (experiment D_{15}). The black arrows show the duration of filter sampling and the corresponding O/C values obtained by XPS analysis. The yellow-highlighted portion of the graph indicates the interval where irradiation takes place, while the green vertical dashed lines indicate the moment of glyoxal injection in the chamber.

https://doi.org/10.5194/egusphere-2024-4073
Preprint. Discussion started: 27 January 2025

Figure 11 shows that the O/C ratio of the organic material in the native dust is around 1.5. During the uptake of glyoxal, the ratio decreases to 1 to finally revert to 1.5 within approximately one hour. The agreement between the measurements of the ACSM and the XPS analysis indicates that the ACSM probes the organic matter at the surface of the particles, which we expect to be involved in the reactivity towards glyoxal. The comparison of the results in Figures 10 and 11 suggests that while glyoxal and high volatility oxidation products evaporate, low volatility and heavy compounds such as oligomers, remains on the dust and modifies in an irreversible way its surface composition. This is in agreement with previous studies carried out on ammonium sulphate seeds (Kroll et al., 2005; Galloway et al., 2009; De Haan et al., 2020; Hu et al., 2022;).

4 Conclusive remarks

In this paper, we investigated the uptake of glyoxal by realistic submicron mineral dust aerosol particles from a natural soil (Gobi Desert), airborne in a large simulation chamber, and aged under variable experimental conditions of relative humidity, irradiation, and ozone concentrations. Results can be summarised and commented as follows:

- The uptake of glyoxal on the dust particles occurs in humid conditions exceeding 30% RH. These observations agree with the results of Liggio et al. (2005a; 2005b) on the uptake of glyoxal on ammonium sulphate aerosols, observing the formation of organic matter only when RH exceeded 50%. Trainic et al. (2011) found that the uptake of glyoxal on glycine and ammonium sulphate particles occurred only when the relative humidity was above 35%. On the contrary, both Shen et al (2016) and Zogka et al. (2024) demonstrated that the uptake can occur in dry conditions too, which we did not observe.

- The uptake of glyoxal on the dust particles starts as soon as the glyoxal is injected in the chamber. In this study we used a single and instantaneous injection of glyoxal, and not a constant steady state flux. Furthermore, in humid conditions, upon injection, glyoxal is partitioned rapidly between the gas phase and the chamber walls. Both facts are actually an advantage to scale our results to ambient conditions. Indeed, Volkamer et al. (2005) estimated that the lifetime of glyoxal in the daytime is of around 1.3 hours. Alvarado et al. (2020) showed that

https://doi.org/10.5194/egusphere-2024-4073
Preprint. Discussion started: 27 January 2025

the long-range transport of glyoxal produced from a point source (Canadian wildfires) may be possible only by invoking the progressive oxidation of its longer-lived precursors in the plume. In the scenario where dust aerosols interact with a glyoxal plume from a point source, one can expect an interaction time of a few minutes, compatible with that of this study.

- At 80% RH, the measured uptake coefficient of glyoxal on mineral dust is $\gamma = (9 \pm 5) \times 10^{-3}$. Because the uptake follows a first order kinetic, the measured uptake coefficient is independent on the glyoxal concentration and transferable to atmospheric conditions. The uptake coefficient on dust is nearly two orders of magnitude higher than for ammonium sulphate ($\gamma_{gas\text{-}AS} = 1.1\ (\pm 0.2) \times 10^{-4}$) at the same relative humidity (our study as well as Curry et al., 2018; De Haan et al., 2020; Galloway et al., 2009; Liggio et al., 2005b, a; Trainic et al., 2011) but lower than $\gamma_{gas\text{-}AS} = 2.9 \times 10^{-3}$ at a lower relative humidity (Liggio et al., 2005).
- The difference could be due to the higher hygroscopicity of ammonium sulphate, enhances water's competition with glyoxal for adsorption sites at 80% RH, when indeed ammonium sulphate is deliquescent. This suggest nonetheless that dust aerosols could play a very substantial role in the formation of organic aerosols at high relative humidity compared to ammonium sulphate, which is often used as an aerosol proxy. Additionally, we found that the uptake coefficient measured by the loss of gas-phase glyoxal molecules agrees very well with the rate of formation of secondary organic mass on the particles. This suggests that the totality of the mass of reacting glyoxal is transformed in organic matter on the surface of the dust particles.
- The uptake of glyoxal and the formation of organic matter last approximately 20 minutes, after which evaporation occurs. However, we demonstrate the uptake of glyoxal modifies irreversibly both the composition and the physical properties of mineral dust. Oligomers and organic acids are detected on the dust even after the uptake has finished. Our findings support several key insights into the irreversible uptake of glyoxal on mineral particles, as discussed by Shen et al. (2016), that found that glyoxal oligomers exhibited a higher degree of oligomerization (≥ 4) than previously reported in the aqueous phase and on acidic seed particles (≤ 3; Liggio et al., 2005a; Nozière et al., 2009) and that adsorbed water on particles favoured the formation of oligomers. This is also in agreement

https://doi.org/10.5194/egusphere-2024-4073
Preprint. Discussion started: 27 January 2025

with the field observations by consistent with the observations conducted by Wang et al. (2015).

- The presence of organic acids, such as glycolic and glyoxylic acids has implications for aerosol pH, as they can influence the acidity of aerosols and their ability to dissolve metals, potentially impacting atmospheric chemistry and the reactivity of aerosol particles (Giorio et al., 2022). Changes in aerosol pH can, in turn, affect the hygroscopic properties of aerosols, influencing their ability to adsorb water and grow in size. Indeed, we observe that the volume of the dust particle increases during the uptake and that this growth is persistent, henceforth becoming more efficient in interacting with visible light and form cloud droplets. The newly formed organic matter from glyoxal on dust particles could also alter the aerosol's optical properties, affecting its ability to absorb solar radiation, as recently observed in aqueous solution (De Haan et al., 2023) or on ammonium sulphate aerosols (De Haan et al. 2020; Trainic et al. 2011). For example, the presence of hydrated glyoxal oligomeric structures has already been observed to have UV radiation absorption properties (Kalberer et al., 2004; Shapiro et al., 2009).

In conclusion, our study reveals a significant quantitative transfer of gas-phase glyoxal molecules to mineral dust aerosol surfaces, occurring within a timescale of a few minutes, underscoring the important role of dust-glyoxal interactions in the atmosphere. Neglecting the uptake pathway on dust could result in an underestimation of glyoxal removal from the atmosphere, potentially leading to disparities between model predictions and observed gaseous concentrations of glyoxal (Kluge et al., 2023; Ling et al., 2020; Volkamer et al., 2007; Washenfelder et al., 2011). The results of this study could have important implications for the aerosol direct and indirect radiative effect and aerosol pH. Further studies should investigate dust from different sources and mineralogy, poly-disperse size distribution including the coarse mode and lower glyoxal concentration.

Data availability. The simulation chamber experiments that support the findings of this study are available through the Database of Atmospheric Simulation Chamber Studies (DASCS) of the EUROCHAMP Data Centre (https:// data.eurochamp.org/ data- access/ chamber- experiments/).

Code availability. The routine used for fitting the size distribution is available at https://doi.org/10.5281/zenodo.8135133 (Baldo and Lu, 2023). Note that in this study we only

https://doi.org/10.5194/egusphere-2024-4073
Preprint. Discussion started: 27 January 2025

used the size distribution measured by the OPC instrument, which was fitted with a lognormal function.

Author contributions. PF, JFD and FB conceptualized the study. PF and FB led the paper writing, with contributions from all the authors. JFD provided with expertise on multi-phase chemistry. CB analysed the aerosol size distribution data. VM supervised the analysis of PTR-MS data. FB and CG performed the ESI-Orbitrap analysis of filter samples. FB and JFB performed the analysis of ACSM observations. FB, TB and AG performed the SFE/CG-MS analysis of filter samples. FB, GN and SC performed the thermo-optical analysis of filter samples. FB, MC, AB, EP, VM, BPV and PF conducted the chamber experiments. MR provided with the soil sample and expertise on heterogeneous chemistry. PF provided with funding.

Competing interests. The authors declare no competing interests.

Special issue statement. This article is not part of a special issue. It is not associated with a conference.

Acknowledgements. The AERIS data center (www.aeris–data.fr) is acknowledged for distributing and curing the data produced by the CESAM chamber through the hosting of the EUROCHAMP data center (https://data.eurochamp.org). The initial contribution of M. Giordano (Afri-SET) to the conceptualisation of the project is gratefully acknowledged.

Financial support. This work has received funding from the French National Research Agency (ANR) though the research project CLIMDO under the grant number ANR-19-CE01-0008-02. It has received support from the European Union's Horizon 2020 research and innovation program through the EUROCHAMP-2020 Infrastructure Activity under grant agreement no. 730997. CNRS-INSU is gratefully acknowledged for supporting the CESAM chamber as a national facility as part of the French ACTRIS Research Infrastructure.

https://doi.org/10.5194/egusphere-2024-4073
Preprint. Discussion started: 27 January 2025

References

Adebiyi, A., Kok, J. F., Murray, B. J., Ryder, C. L., Stuut, J.-B. W., Kahn, R. A., Knippertz, P., Formenti, P., Mahowald, N. M., Pérez García-Pando, C., Klose, M., Ansmann, A., Samset, B. H., Ito, A., Balkanski, Y., Di Biagio, C., Romanias, M. N., Huang, Y., and Meng, J.: A review of coarse mineral dust in the Earth system, Aeol. Res., 60, 100849, https://doi.org/10.1016/j.aeolia.2022.100849, 2023.

Aiken, A. C., DeCarlo, P. F., Kroll, J. H., Worsnop, D. R., Huffman, J. A., Docherty, K. S., Ulbrich, I. M., Mohr, C., Kimmel, J. R., Sueper, D., Sun, Y., Zhang, Q., Trimborn, A., Northway, M., Ziemann, P. J., Canagaratna, M. R., Onasch, T. B., Alfarra, M. R., Prevot, A. S. H., Dommen, J., Duplissy, J., Metzger, A., Baltensperger, U., and Jimenez, J. L.: O/C and OM/OC Ratios of Primary, Secondary, and Ambient Organic Aerosols with High-Resolution Time-of-Flight Aerosol Mass Spectrometry, Environ. Sci. Technol., 42, 4478–4485, https://doi.org/10.1021/es703009q, 2008.

Baldo, C., Formenti, P., Di Biagio, C., Lu, G., Song, C., Cazaunau, M., Pangui, E., Doussin, J.-F., Dagsson-Waldhauserova, P., Arnalds, O., Beddows, D., MacKenzie, A. R., and Shi, Z.: Complex refractive index and single scattering albedo of Icelandic dust in the shortwave part of the spectrum, Atmos. Chem. Phys., 23, 7975–8000, https://doi.org/10.5194/acp-23-7975-2023, 2023.

Baldo, C. and G. Lu. (2023). Research code supporting "Complex refractive index and single scattering albedo of Icelandic dust in the shortwave spectrum" (v1.0.0). Zenodo. https://doi.org/10.5281/zenodo.8135133

Bauer, S. E., Mishchenko, M. I., Lacis, A. A., Zhang, S., Perlwitz, J., and Metzger, S. M.: Do sulfate and nitrate coatings on mineral dust have important effects on radiative properties and climate modeling?, J. Geophys. Res., 112, D06307, https://doi.org/10.1029/2005JD006977, 2007.

Brégonzio-Rozier, L., Giorio, C., Siekmann, F., Pangui, E., Morales, S. B., Temime-Roussel, B., Gratien, A., Michoud, V., Cazaunau, M., DeWitt, H. L., Tapparo, A., Monod, A., and Doussin, J.-F.: Secondary organic aerosol formation from isoprene photooxidation during cloud condensation–evaporation cycles, Atmos. Chem. Phys., 16, 1747–1760, https://doi.org/10.5194/acp-16-1747-2016, 2016.

Buxton, G. V., Malone, T. N., and Arthur Salmon, G.: Oxidation of glyoxal initiated by OH in oxygenated aqueous solution, Faraday Trans., 93, 2889–2891, https://doi.org/10.1039/a701468f, 1997.

Carlton, A. G., Turpin, B. J., Altieri, K. E., Seitzinger, S., Reff, A., Lim, H.-J., and Ervens, B.: Atmospheric oxalic acid and OA production from glyoxal: Results of aqueous photooxidation experiments, Atmos. Environ., 41, 7588–7602, https://doi.org/10.1016/j.atmosenv.2007.05.035, 2007.

Castellanos, P., Colarco, P., Espinosa, W. R., Guzewich, S. D., Levy, R. C., Miller, R. L., Chin, M., Kahn, R. A., Kemppinen, O., Moosmüller, H., Nowottnick, E. P., Rocha-Lima, A., Smith, M. D., Yorks, J. E., and Yu, H.: Mineral dust optical properties for remote sensing and global modeling: A review, Remote Sensing of Environment, 303, 113982, https://doi.org/10.1016/j.rse.2023.113982, 2024.

Chan Miller, C., Jacob, D. J., Marais, E. A., Yu, K., Travis, K. R., Kim, P. S., Fisher, J. A., Zhu, L., Wolfe, G. M., Hanisco, T. F., Keutsch, F. N., Kaiser, J., Min, K.-E., Brown, S. S., Washenfelder, R. A., González Abad, G., and Chance, K.: Glyoxal yield from isoprene oxidation and relation to formaldehyde: chemical mechanism, constraints from SENEX aircraft observations, and interpretation of OMI satellite data, Atmos. Chem. Phys., 17, 8725–8738, https://doi.org/10.5194/acp-17-8725-2017, 2017.

Chen, S., Chen, J., Zhang, Y., Lin, J., Bi, H., Song, H., Chen, Y., Lian, L., Liu, C., and Zhang, R.: Anthropogenic dust: sources, characteristics and emissions, Environ. Res. Lett., 18, 103002, https://doi.org/10.1088/1748-9326/acf479, 2023.

Chiappini, L., Perraudin, E., Durand-Jolibois, R., and Doussin, J. F.: Development of a supercritical fluid extraction–gas chromatography–mass spectrometry method for the identification of highly polar compounds in secondary organic aerosols formed from biogenic hydrocarbons in smog chamber experiments, Anal. Bioanal. Chem., 386, 1749–1759, https://doi.org/10.1007/s00216-006-0744-3, 2006.

https://doi.org/10.5194/egusphere-2024-4073
Preprint. Discussion started: 27 January 2025

Chirizzi, D., Cesari, D., Guascito, M. R., Dinoi, A., Giotta, L., Donateo, A., and Contini, D., Influence of Saharan dust outbreaks and carbon content on oxidative potential of water-soluble fractions of PM2. 5 and PM10. Atmos. Environ., 163, 1-8, 2017

Crowley, J. N., Ammann, M., Cox, R. A., Hynes, R. G., Jenkin, M. E., Mellouki, A., Rossi, M. J., Troe, J., and Wallington, T. J.: Evaluated kinetic and photochemical data for atmospheric chemistry: Volume V – heterogeneous reactions on solid substrates, Atmos. Chem. Phys., 10, 9059–9223, https://doi.org/10.5194/acp-10-9059-2010, 2010.

Curry, L. A., Tsui, W. G., and McNeill, V. F.: Technical note: Updated parameterization of the reactive uptake of glyoxal and methylglyoxal by atmospheric aerosols and cloud droplets, Atmos. Chem. Phys., 18, 9823–9830, https://doi.org/10.5194/acp-18-9823-2018, 2018.

De Haan, D. O., Hawkins, L. N., Jansen, K., Welsh, H. G., Pednekar, R., De Loera, A., Jimenez, N. G., Tolbert, M. A., Cazaunau, M., Gratien, A., Bergé, A., Pangui, E., Formenti, P., and Doussin, J.-F.: Glyoxal's impact on dry ammonium salts: fast and reversible surface aerosol browning, Atmos. Chem. Phys., 20, 9581–9590, https://doi.org/10.5194/acp-20-9581-2020, 2020.

De Haan, D. O., Hawkins, L. N., Wickremasinghe, P. D., Andretta, A. D., Dignum, J. R., De Haan, A. C., Welsh, H. G., Pennington, E. A., Cui, T., Surratt, J. D., Cazaunau, M., Pangui, E., and Doussin, J.-F.: Brown Carbon from Photo-Oxidation of Glyoxal and SO_2 in Aqueous Aerosol, ACS Earth Space Chem., 7, 1131–1140, https://doi.org/10.1021/acsearthspacechem.3c00035, 2023.

Denjean, C., Formenti, P., Picquet-Varrault, B., Katrib, Y., Pangui, E., Zapf, P., and Doussin, J. F.: A new experimental approach to study the hygroscopic and optical properties of aerosols: application to ammonium sulfate particles, Atmos. Meas. Tech., 7, 183–197, https://doi.org/10.5194/amt-7-183-2014, 2014.

Di Biagio, C., Formenti, P., Balkanski, Y., Caponi, L., Cazaunau, M., Pangui, E., Journet, E., Nowak, S., Caquineau, S., Andreae, M. O., Kandler, K., Saeed, T., Piketh, S., Seibert, D., Williams, E., and Doussin, J.-F.: Global scale variability of the mineral dust long-wave refractive index: a new dataset of in situ measurements for climate modeling and remote sensing, Atmos. Chem. Phys., 17, 1901–1929, https://doi.org/10.5194/acp-17-1901-2017, 2017.

Di Biagio, C., Formenti, P., Balkanski, Y., Caponi, L., Cazaunau, M., Pangui, E., Journet, E., Nowak, S., Andreae, M. O., Kandler, K., Saeed, T., Piketh, S., Seibert, D., Williams, E., and Doussin, J.-F.: Complex refractive indices and single-scattering albedo of global dust aerosols in the shortwave spectrum and relationship to size and iron content, Atmos. Chem. Phys., 19, 15503–15531, https://doi.org/10.5194/acp-19-15503-2019, 2019.

Dupart, Y., King, S. M., Nekat, B., Nowak, A., Wiedensohler, A., Herrmann, H., David, G., Thomas, B., Miffre, A., Rairoux, P., D'Anna, B., and George, C.: Mineral dust photochemistry induces nucleation events in the presence of SO_2, Proc. Natl. Acad. Sci. U.S.A., 109, 20842–20847, https://doi.org/10.1073/pnas.1212297109, 2012.

Ervens, B. and Volkamer, R.: Glyoxal processing by aerosol multiphase chemistry: towards a kinetic modeling framework of secondary organic aerosol formation in aqueous particles, Atmos. Chem. Phys., 10, 8219–8244, https://doi.org/10.5194/acp-10-8219-2010, 2010.

Fu, T.-M., Jacob, D. J., Wittrock, F., Burrows, J. P., Vrekoussis, M., and Henze, D. K.: Global budgets of atmospheric glyoxal and methylglyoxal, and implications for formation of secondary organic aerosols, J. Geophys. Res., 113, D15303, https://doi.org/10.1029/2007JD009505, 2008.

Galloway, M. M., Chhabra, P. S., Chan, A. W. H., Surratt, J. D., Flagan, R. C., Seinfeld, J. H., and Keutsch, F. N.: Glyoxal uptake on ammonium sulphate seed aerosol: reaction products and reversibility of uptake under dark and irradiated conditions, Atmos. Chem. Phys., 2009.

Giorio, C., Monod, A., Brégonzio-Rozier, L., DeWitt, H. L., Cazaunau, M., Temime-Roussel, B., Gratien, A., Michoud, V., Pangui, E., Ravier, S., Zielinski, A. T., Tapparo, A., Vermeylen, R., Claeys, M., Voisin, D., Kalberer, M., and Doussin, J.-F.: Cloud Processing of Secondary Organic Aerosol from Isoprene and Methacrolein Photooxidation, J. Phys. Chem. A, 121, 7641–7654, https://doi.org/10.1021/acs.jpca.7b05933, 2017.

Giorio, C., D'Aronco, S., Di Marco, V., Badocco, D., Battaglia, F., Soldà, L., Pastore, P., and Tapparo, A.: Emerging investigator series: aqueous-phase processing of atmospheric aerosol influences dissolution kinetics of metal ions in an urban background site in the Po Valley, Environ. Sci.: Processes Impacts, 24, 884–897, https://doi.org/10.1039/D2EM00023G, 2022.

Goodman, A. L., Underwood, G. M., and Grassian, V. H.: Heterogeneous Reaction of NO2 : Characterization of Gas-Phase and Adsorbed Products from the Reaction, 2NO2(g) + H2O(a) → HONO(g) + HNO3(a) on Hydrated Silica Particles, J. Phys. Chem. A, 103, 7217–7223, https://doi.org/10.1021/jp9910688, 1999.

Guo, Y., Wang, S., Zhu, J., Zhang, R., Gao, S., Saiz-Lopez, A., and Zhou, B.: Atmospheric formaldehyde, glyoxal and their relations to ozone pollution under low- and high-NOx regimes in summertime Shanghai, China, Atmos. Res., 258, 105635, https://doi.org/10.1016/j.atmosres.2021.105635, 2021.

Hettiarachchi, E. and Grassian, V. H.: Heterogeneous Reactions of Phenol on Different Components of Mineral Dust Aerosol: Formation of Oxidized Organic and Nitro-Phenolic Compounds, ACS EST Air, 1, 259–272, https://doi.org/10.1021/acsestair.3c00042, 2024.

Horowitz, A., Meller, R., & Moortgat, G. K. (2001). The UV–VIS absorption cross sections of the α-dicarbonyl compounds: pyruvic acid, biacetyl and glyoxal. J. Photochem. Photobiol., A, 146(1-2), 19-27.

Hu, J., Chen, Z., Qin, X., and Dong, P.: Reversible and irreversible gas–particle partitioning of dicarbonyl compounds observed in the real atmosphere, Atmos. Chem. Phys., 22, 6971–6987, https://doi.org/10.5194/acp-22-6971-2022, 2022.

Joshi, N., Romanias, M. N., Riffault, V., and Thevenet, F.: Investigating water adsorption onto natural mineral dust particles: Linking DRIFTS experiments and BET theory, Aeolian Res, 27, 35–45, https://doi.org/10.1016/j.aeolia.2017.06.001, 2017.

Lai, A. C., Nazaroff, W. W., Modeling indoor particle deposition from turbulent flow onto smooth surfaces. J. Aerosol Sci., 31, 463-476, 2000.

Kalberer, M., Paulsen, D., Sax, M., Steinbacher, M., Dommen, J., Prevot, A. S. H., Fisseha, R., Weingartner, E., Frankevich, V., Zenobi, R., and Baltensperger, U.: Identification of Polymers as Major Components of Atmospheric Organic Aerosols, Science, 303, 1659–1662, https://doi.org/10.1126/science.1092185, 2004.

Kluge, F., Hüneke, T., Lerot, C., Rosanka, S., Rotermund, M. K., Taraborrelli, D., Weyland, B., and Pfeilsticker, K.: Airborne glyoxal measurements in the marine and continental atmosphere: comparison with TROPOMI observations and EMAC simulations, Atmos. Chem. Phys., 23, 1369–1401, https://doi.org/10.5194/acp-23-1369-2023, 2023.

Knippertz, P. and Stuut, J.-B. W. (Eds.): Mineral Dust: A Key Player in the Earth System, Springer Netherlands, Dordrecht, https://doi.org/10.1007/978-94-017-8978-3, 2014.

Knote, C., Hodzic, A., Jimenez, J. L., Volkamer, R., Orlando, J. J., Baidar, S., Brioude, J., Fast, J., Gentner, D. R., Goldstein, A. H., Hayes, P. L., Knighton, W. B., Oetjen, H., Setyan, A., Stark, H., Thalman, R., Tyndall, G., Washenfelder, R., Waxman, E., and Zhang, Q.: Simulation of semi-explicit mechanisms of OA formation from glyoxal in aerosol in a 3-D model, Atmos. Chem. Phys., 14, 6213–6239, https://doi.org/10.5194/acp-14-6213-2014, 2014.

Kok, J. F., Adebiyi, A. A., Albani, S., Balkanski, Y., Checa-Garcia, R., Chin, M., Colarco, P. R., Hamilton, D. S., Huang, Y., Ito, A., Klose, M., Li, L., Mahowald, N. M., Miller, R. L., Obiso, V., Pérez García-Pando, C., Rocha-Lima, A., and Wan, J. S.: Contribution of the world's main dust source regions to the global cycle of desert dust, Aerosols/Atmospheric Modelling/Troposphere/Physics (physical properties and processes), https://doi.org/10.5194/acp-2021-4, 2021.

Kok, J. F., Storelvmo, T., Karydis, V. A., Adebiyi, A. A., Mahowald, N. M., Evan, A. T., He, C., and Leung, D. M.: Mineral dust aerosol impacts on global climate and climate change, Nat Rev Earth Environ, 4, 71–86, https://doi.org/10.1038/s43017-022-00379-5, 2023.

Kourtchev, I., Doussin, J.-F., Giorio, C., Mahon, B., Wilson, E. M., Maurin, N., Pangui, E., Venables, D. S., Wenger, J. C., and Kalberer, M.: Molecular composition of fresh and aged secondary organic

aerosol from a mixture of biogenic volatile compounds: a high-resolution mass spectrometry study, Atmos. Chem. Phys., 15, 5683–5695, https://doi.org/10.5194/acp-15-5683-2015, 2015.

Kroll, J. H., Ng, N. L., Murphy, S. M., Varutbangkul, V., Flagan, R. C., and Seinfeld, J. H.: Chamber studies of secondary organic aerosol growth by reactive uptake of simple carbonyl compounds, J. Geophys. Res., 110, 2005JD006004, https://doi.org/10.1029/2005JD006004, 2005.

Lewis, A. C., Hopkins, J. R., Carslaw, D. C., Hamilton, J. F., Nelson, B. S., Stewart, G., Dernie, J., Passant, N., and Murrells, T.: An increasing role for solvent emissions and implications for future measurements of volatile organic compounds, Phil. Trans. R. Soc. A., 378, 20190328, https://doi.org/10.1098/rsta.2019.0328, 2020.

Li, L., Mahowald, N. M., Miller, R. L., Pérez García-Pando, C., Klose, M., Hamilton, D. S., Gonçalves Ageitos, M., Ginoux, P., Balkanski, Y., Green, R. O., Kalashnikova, O., Kok, J. F., Obiso, V., Paynter, D., and Thompson, D. R.: Quantifying the range of the dust direct radiative effect due to source mineralogy uncertainty, Atmos. Chem. Phys., 21, 3973–4005, https://doi.org/10.5194/acp-21-3973-2021, 2021.

Li, Q., Gong, D., Wang, H., Wang, Y., Han, S., Wu, G., Deng, S., Yu, P., Wang, W., and Wang, B.: Rapid increase in atmospheric glyoxal and methylglyoxal concentrations in Lhasa, Tibetan Plateau: Potential sources and implications, Sci. Total Environ., 824, 153782, https://doi.org/10.1016/j.scitotenv.2022.153782, 2022.

Liggio, J., Li, S.-M., and McLaren, R.: Heterogeneous Reactions of Glyoxal on Particulate Matter: Identification of Acetals and Sulfate Esters, Environ. Sci. Technol., 39, 1532–1541, https://doi.org/10.1021/es048375y, 2005a.

Liggio, J., Li, S., and McLaren, R.: Reactive uptake of glyoxal by particulate matter, J. Geophys. Res., 110, 2004JD005113, https://doi.org/10.1029/2004JD005113, 2005b.

Lim, Y. B., Tan, Y., Perri, M. J., Seitzinger, S. P., and Turpin, B. J.: Aqueous chemistry and its role in secondary organic aerosol (OA) formation, Atmos. Chem. Phys., 10, 10521–10539, https://doi.org/10.5194/acp-10-10521-2010, 2010.

Ling, Z., Xie, Q., Shao, M., Wang, Z., Wang, T., Guo, H., and Wang, X.: Formation and sink of glyoxal and methylglyoxal in a polluted subtropical environment: observation-based photochemical analysis and impact evaluation, Atmos. Chem. Phys., 20, 11451–11467, https://doi.org/10.5194/acp-20-11451-2020, 2020.

Liu, C., Chu, B., Liu, Y., Ma, Q., Ma, J., He, H., Li, J., and Hao, J.: Effect of mineral dust on secondary organic aerosol yield and aerosol size in α-pinene/NOx photo-oxidation, Atmos. Environ., 77, 781–789, https://doi.org/10.1016/j.atmosenv.2013.05.064, 2013.

Mahowald, N., Albani, S., Kok, J. F., Engelstaeder, S., Scanza, R., Ward, D. S., and Flanner, M. G.: The size distribution of desert dust aerosols and its impact on the Earth system, Aeolian Research, 15, 53–71, https://doi.org/10.1016/j.aeolia.2013.09.002, 2014.

Nault, B. A., Croteau, P., Jayne, J., Williams, A., Williams, L., Worsnop, D., Katz, E. F., DeCarlo, P. F., and Canagaratna, M.: Laboratory evaluation of organic aerosol relative ionization efficiencies in the aerodyne aerosol mass spectrometer and aerosol chemical speciation monitor, Aerosol Science and Technology, 57, 981–997, https://doi.org/10.1080/02786826.2023.2223249, 2023.

Ng, N. L., Canagaratna, M. R., Jimenez, J. L., Chhabra, P. S., Seinfeld, J. H., and Worsnop, D. R.: Changes in organic aerosol composition with aging inferred from aerosol mass spectra, Atmos. Chem. Phys., 11, 6465–6474, https://doi.org/10.5194/acp-11-6465-2011, 2011.

Nie, W., Ding, A., Wang, T., Kerminen, V.-M., George, C., Xue, L., Wang, W., Zhang, Q., Petäjä, T., Qi, X., Gao, X., Wang, X., Yang, X., Fu, C., and Kulmala, M.: Polluted dust promotes new particle formation and growth, Sci Rep, 4, 6634, https://doi.org/10.1038/srep06634, 2014.

Nieder, R., Benbi, D. K., and Reichl, F. X.: Soil-Borne Particles and Their Impact on Environment and Human Health, in: Soil Components and Human Health, Springer Netherlands, Dordrecht, 99–177, https://doi.org/10.1007/978-94-024-1222-2_3, 2018.

https://doi.org/10.5194/egusphere-2024-4073
Preprint. Discussion started: 27 January 2025

Nozière, B., Dziedzic, P., and Córdova, A.: Products and Kinetics of the Liquid-Phase Reaction of Glyoxal Catalyzed by Ammonium Ions (NH4+), J. Phys. Chem. A, 113, 231–237, https://doi.org/10.1021/jp8078293, 2009.

Ooki, A. and Uematsu, M.: Chemical interactions between mineral dust particles and acid gases during Asian dust events, J. Geophys. Res., 110, 2004JD004737, https://doi.org/10.1029/2004JD004737, 2005.

Patriarca, C., Bergquist, J., Sjöberg, P. J. R., Tranvik, L., and Hawkes, J. A.: Online HPLC-ESI-HRMS Method for the Analysis and Comparison of Different Dissolved Organic Matter Samples, Environ. Sci. Technol., 52, 2091–2099, https://doi.org/10.1021/acs.est.7b04508, 2018.

Ponczek, M., Hayeck, N., Emmelin, C., and George, C.: Heterogeneous photochemistry of dicarboxylic acids on mineral dust, Atmos. Environ., 212, 262–271, https://doi.org/10.1016/j.atmosenv.2019.05.032, 2019.

Romanias, M. N., El Zein, A., and Bedjanian, Y.: Heterogeneous Interaction of H_2O_2 with TiO_2 Surface under Dark and UV Light Irradiation Conditions, J. Phys. Chem. A, 116, 8191–8200, https://doi.org/10.1021/jp305366v, 2012.

Rossignol, S., Aregahegn, K. Z., Tinel, L., Fine, L., Nozière, B., and George, C.: Glyoxal Induced Atmospheric Photosensitized Chemistry Leading to Organic Aerosol Growth, Environ. Sci. Technol., 48, 3218–3227, https://doi.org/10.1021/es405581g, 2014.

Rubasinghege, G., Ogden, S., Baltrusaitis, J., and Grassian, V. H.: Heterogeneous Uptake and Adsorption of Gas-Phase Formic Acid on Oxide and Clay Particle Surfaces: The Roles of Surface Hydroxyl Groups and Adsorbed Water in Formic Acid Adsorption and the Impact of Formic Acid Adsorption on Water Uptake, J. Phys. Chem. A, 117, 11316–11327, https://doi.org/10.1021/jp408169w, 2013.

Safi Shalamzari, M., Ryabtsova, O., Kahnt, A., Vermeylen, R., Hérent, M., Quetin-Leclercq, J., Van Der Veken, P., Maenhaut, W., and Claeys, M.: Mass spectrometric characterization of organosulfates related to secondary organic aerosol from isoprene, Rapid Comm Mass Spectrometry, 27, 784–794, https://doi.org/10.1002/rcm.6511, 2013.

Seisel, S., Lian, Y., Keil, T., Trukhin, M. E., and Zellner, R.: Kinetics of the interaction of water vapour with mineral dust and soot surfaces at T = 298 K, Phys. Chem. Chem. Phys., 6, 1926–1932, https://doi.org/10.1039/B314568A, 2004.

Shapiro, E. L., Szprengiel, J., Sareen, N., Jen, C. N., Giordano, M. R., and McNeill, V. F.: Light-absorbing secondary organic material formed by glyoxal in aqueous aerosol mimics, Atmos. Chem. Phys., 9, 2289–2300, https://doi.org/10.5194/acp-9-2289-2009, 2009.

Shen, X., Wu, H., Zhao, Y., Huang, D., Huang, L., and Chen, Z.: Heterogeneous reactions of glyoxal on mineral particles: A new avenue for oligomers and organosulfate formation, Atmos. Environ., 131, 133–140, https://doi.org/10.1016/j.atmosenv.2016.01.048, 2016.

Shrivastava, M., Cappa, C. D., Fan, J., Goldstein, A. H., Guenther, A. B., Jimenez, J. L., Kuang, C., Laskin, A., Martin, S. T., Ng, N. L., Petaja, T., Pierce, J. R., Rasch, P. J., Roldin, P., Seinfeld, J. H., Shilling, J., Smith, J. N., Thornton, J. A., Volkamer, R., Wang, J., Worsnop, D. R., Zaveri, R. A., Zelenyuk, A., and Zhang, Q.: Recent advances in understanding secondary organic aerosol: Implications for global climate forcing, Rev. Geophys., 55, 509–559, https://doi.org/10.1002/2016RG000540, 2017.

Sun, Y. L., Zhang, Q., Anastasio, C., and Sun, J.: Insights into secondary organic aerosol formed via aqueous-phase reactions of phenolic compounds based on high resolution mass spectrometry, Atmos. Chem. Phys., 10, 4809–4822, https://doi.org/10.5194/acp-10-4809-2010, 2010.

Tang, M., Huang, X., Lu, K., Ge, M., Li, Y., Cheng, P., Zhu, T., Ding, A., Zhang, Y., Gligorovski, S., Song, W., Ding, X., Bi, X., and Wang, X.: Heterogeneous reactions of mineral dust aerosol: implications for tropospheric oxidation capacity, Atmos. Chem. Phys., 17, 11727–11777, https://doi.org/10.5194/acp-17-11727-2017, 2017.

Tegen, I. and Fung, I.: Contribution to the atmospheric mineral aerosol load from land surface modification, J. Geophys. Res., 100, 18707, https://doi.org/10.1029/95JD02051, 1995.

https://doi.org/10.5194/egusphere-2024-4073
Preprint. Discussion started: 27 January 2025

Trainic, M., Abo Riziq, A., Lavi, A., Flores, J. M., and Rudich, Y.: The optical, physical and chemical properties of the products of glyoxal uptake on ammonium sulfate seed aerosols, Atmos. Chem. Phys., 11, 9697–9707, https://doi.org/10.5194/acp-11-9697-2011, 2011.

Turpin, B. J. and Huntzicker, J. J.: Identification of secondary organic aerosol episodes and quantitation of primary and secondary organic aerosol concentrations during SCAQS, Atmos. Environ., 29, 3527–3544, https://doi.org/10.1016/1352-2310(94)00276-Q, 1995.

Usher, C. R., Michel, A. E., and Grassian, V. H.: Reactions on Mineral Dust, Chem. Rev., 103, 4883–4940, https://doi.org/10.1021/cr020657y, 2003.

Volkamer, R., Platt, U., and Wirtz, K.: Primary and Secondary Glyoxal Formation from Aromatics: Experimental Evidence for the Bicycloalkyl−Radical Pathway from Benzene, Toluene, and p -Xylene, J. Phys. Chem. A, 105, 7865–7874, https://doi.org/10.1021/jp010152w, 2001.

Volkamer, R., San Martini, F., Molina, L. T., Salcedo, D., Jimenez, J. L., and Molina, M. J.: A missing sink for gas-phase glyoxal in Mexico City: Formation of secondary organic aerosol, Geophysical Research Letters, 34, 2007GL030752, https://doi.org/10.1029/2007GL030752, 2007.

Vrekoussis, M., Wittrock, F., Richter, A., Burrows, J. P., and Cho, C.: Temporal and spatial variability of glyoxal as observed from space, Atmos. Chem. Phys., 2009.

Wagner, C., Hanisch, F., Holmes, N., de Coninck, H., Schuster, G., and Crowley, J. N.: The interaction of N_2O_5 with mineral dust: aerosol flow tube and Knudsen reactor studies, Atmos. Chem. Phys., 2008.

Walker, H., Stone, D., Ingham, T., Hackenberg, S., Cryer, D., Punjabi, S., Read, K., Lee, J., Whalley, L., Spracklen, D. V., Carpenter, L. J., Arnold, S. R., and Heard, D. E.: Observations and modelling of glyoxal in the tropical Atlantic marine boundary layer, Atmos. Chem. Phys., 22, 5535–5557, https://doi.org/10.5194/acp-22-5535-2022, 2022.

Wang, G., Cheng, C., Meng, J., Huang, Y., Li, J., and Ren, Y.: Field observation on secondary organic aerosols during Asian dust storm periods: Formation mechanism of oxalic acid and related compounds on dust surface, Atmos. Environ., 113, 169–176, https://doi.org/10.1016/j.atmosenv.2015.05.013, 2015.

Washenfelder, R. A., Young, C. J., Brown, S. S., Angevine, W. M., Atlas, E. L., Blake, D. R., Bon, D. M., Cubison, M. J., De Gouw, J. A., Dusanter, S., Flynn, J., Gilman, J. B., Graus, M., Griffith, S., Grossberg, N., Hayes, P. L., Jimenez, J. L., Kuster, W. C., Lefer, B. L., Pollack, I. B., Ryerson, T. B., Stark, H., Stevens, P. S., and Trainer, M. K.: The glyoxal budget and its contribution to organic aerosol for Los Angeles, California, during CalNex 2010: Glyoxal Budget for Los Angeles, J. Geophys. Res., 116, https://doi.org/10.1029/2011JD016314, 2011.

Webb, N. P. and Pierre, C.: Quantifying Anthropogenic Dust Emissions, Earth's Future, 6, 286–295, https://doi.org/10.1002/2017EF000766, 2018.

Zeineddine, M. N., Romanias, M. N., Gaudion, V., Riffault, V., and Thévenet, F.: Heterogeneous Interaction of Isoprene with Natural Gobi Dust, ACS Earth Space Chem., 1, 236–243, https://doi.org/10.1021/acsearthspacechem.7b00050, 2017.

Zielinski, A. T., Kourtchev, I., Bortolini, C., Fuller, S. J., Giorio, C., Popoola, O. A. M., Bogialli, S., Tapparo, A., Jones, R. L., and Kalberer, M.: A new processing scheme for ultra-high resolution direct infusion mass spectrometry data, Atmos. Environ., 178, 129–139, https://doi.org/10.1016/j.atmosenv.2018.01.034, 2018.

Zogka, A. G., Lostier, A., Papadimitriou, V. C., Thevenet, F., Formenti, P., Rossi, M. J., Chen, H., and Romanias, M. N.: Unraveling the Uptake of Glyoxal on a Diversity of Natural Dusts and Surrogates: Linking Dust Composition to Glyoxal Uptake and Estimation of Atmospheric Lifetimes, ACS Earth Space Chem., 8, 1165–1178, https://doi.org/10.1021/acsearthspacechem.3c00359, 2024.